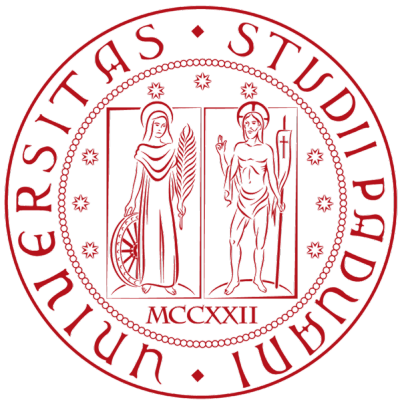

Università degli Studi di Padova

Dipartimento di Fisica e Astronomia "Galileo Galilei"
Corso di Laurea in Fisica

Optimization of an adaptive thermal lensing device for ground-based gravitational waves interferometers

Laureando:
Giacomo Galloni
Matricola 1097826

Relatore:
Dr. Giacomo Ciani

Anno Accademico 2017-2018

Contents

Introduction **v**

1 Background **1**
1.1 The Mode Matching Problem . . . 1
1.1.1 Optical Cavities and Lasers modes . . . 1
1.1.2 Thermal Adaptive Lensing . . . 4
1.2 Gravitational Waves . . . 7
1.2.1 Detection of Gravitational Waves . . . 8
1.3 *LIGO* . . . 9
1.3.1 Operating principles and layout . . . 9
1.3.2 LIGO Sensitivity Limits . . . 10
1.3.3 Quantum Noise and Squeezed Light . . . 12

2 Previous Projects **15**
2.1 Prototype 1 . . . 15
2.1.1 Holders, Heaters and the Lens . . . 15
2.1.2 Results and Issues . . . 16
2.2 Prototype 2.0 . . . 18
2.2.1 Heaters . . . 18
2.2.2 Holders and their Positioning . . . 19
2.2.3 Issues . . . 21

3 Prototype 2.1 **23**
3.1 Holders and their Positioning . . . 23
3.1.1 Design . . . 23
3.1.2 Material . . . 24
3.2 New Heaters . . . 25
3.3 Electrical Contacts . . . 28

4 Testing and Data Analysis **31**
4.1 Functional Tests . . . 31
4.2 Beam Scan . . . 34
4.3 Optical Path and Setup . . . 35

4.4 Beam Scans 36
4.5 Results 40

5 Conclusions **45**
5.1 Structural and Mechanical Aspects 45
5.2 Thermal Efficiency and Uniformity 46
5.3 Future Works 46

Bibliography **49**

Introduction

Thermal Lensing is defined as a lensing effect induced on an optical element (OE) by temperature gradients. Indeed, the heat flux on an OE coming from an incident beam, or some other external source, will result in optical path deformations governed by the mechanical and optical characteristics of the OE, such as the coefficient of linear expansion and the thermo-refractive coefficient. This phenomenon applied intentionally on an OE generate an adaptive optical element (AOE), that can be shaped to suit the requirements of an experiment by controlling actively the thermal gradients. These devices find a multitude of applications in many research fields, but I will concentrate on their usage on the matching process of an optical cavity.
In this thesis, I will explain how *Thermal Lensing* can be functional to the successful implementation of other technologies which can increase the already incredible sensitivity of laser interferometers for the detection of gravitational waves (GW), in particular *LIGO*.
These years represent the birth of the GW-exploration of the universe with the six events of merging black holes observed so far and the most recent, and most astonishing, observation of a merging system of two neutron stars. GW represent a whole new perspective from which to observe astronomical objects, that has brought to the so called *multimessenger astrophysics*, that studies the data coming from sources that emits both electromagnetic and gravitational waves.
To improve our capacity of observing these extremely violent events happening hundreds of millions of light years away, we have to push further the sensitivity of our interferometers. One of the main noise sources for these instruments is quantum noise, which is a combination of quantum radiation pressure, dominating at low frequency, and shot noise, dominating at high frequency. One way to reduce quantum noise is by employing *vacuum squeezing* techniques, which relies on the manipulation of the uncertainty in the quantum observables that describe the electromagnetic field. However, to be able to use it efficiently, we need to limit, or even eliminate, all the power losses in the optical path of the laser beam.
Optical losses can arise from the mode-match process and need to be compensated by a suitable lensing device.
Since the matching conditions change through time, because of thermal lensing, it is necessary to use a device capable of changing actively its characteristics. Adaptive lenses, which also exploit thermal lensing, are indeed used to dynamically correct the defects on the matching. the thermal lensing device analysed in this thesis is able to modify its

focal length and its astigmatic and steering ability depending on the temperature gradient provided by some external source of heat.
It represents an excellent way to limit or eliminate optical losses coming from the matching process, allowing to efficiently implement techniques such as the *Squeezing*, which will improve the performances of ground-based gravitational waves interferometers.

In this thesis I will introduce how the theory of the *General Relativity* predicts *GW* and how we were able to detect them in this later years thanks to *LIGO* interferometers, which will be analysed; I will also relate some necessary theoretical explanations on laser beams, optical cavities and on the so-called *Mismatch problem*. Secondly, I will describe the state of the art of *AOE* developed since 2010 at *University of Florida*'s (*UF*) laboratories. Finally, I will describe the new prototype we developed, pointing out its strengths and weaknesses.

Chapter 1

Background

1.1 The Mode Matching Problem

Before talking about GW and ground-based interferometers, we need to introduce lasers and optical cavities, in order to analyse the mode matching problem, which represent the core purpose of this thesis.

1.1.1 Optical Cavities and Lasers modes

An optical cavity, or optical resonator, can be considered a light confinement system made of two or more mirrors, that makes a light wave reflect over a closed path.
The most simple example consists of two mirrors aligned along a specific direction, that is assumed to be the optical axis. Both the mirrors have a specific transmissivity that defines the probability of a photon to pass or to be reflected.
For a particular relation between the length of the cavity and the wavelength, after a round-trip the light interferes constructively with itself and a resonant condition is achieved. For this to happen however, the beam also has to come back after a round trip with the same transverse intensity and phase profiles. This condition defines the so-called spatial modes. They describe specific transverse intensity and phase profiles of a beam, and constitute the elements of different orthonormal basis that can be used to describe a generic laser beam. Usually the most used basis are the Hermite-Gaussian modes and the Laguerre-Gaussian modes, characterized by rectangular or cylindrical symmetry and described by using respectively cartesian (x, y) and angular coordinates (r, θ).
Indeed, the electromagnetic field equation in free space is:

$$[\nabla^2 + k^2]E(x, y, z) = 0 \tag{1.1}$$

We can also extract the primary propagation factor from $E(x, y, z)$ resulting in:

$$E(x, y, z) = u(x, y, z)e^{-ikz} \tag{1.2}$$

where $u(x, y, z)$ is the complex scalar wave amplitude which describes the transverse propagation of the beam. It has to satisfy the following equation, in which we have applied the

paraxial approximation (i.e. confined to a small region around the optical axis) to remove the second partial derivative in z:

$$\nabla_t^2 u(s,z) - 2ik\frac{\partial u(s,t)}{\partial z} = 0 \tag{1.3}$$

here s refers to the transverse coordinates (x,y) or (r,θ) and ∇_t^2 means the laplacian operator operating on these coordinates in the transverse plane.
After some further manipulation and using the Fresnel approximation of diffraction it is possible to obtain the lowest order solution, which represents a *gaussian beam*:

$$u(x,y,z) = \frac{1}{R(z)} exp[-ik\frac{(x-x_0)^2+(y-y_0)^2}{2R(z)}] \tag{1.4}$$

where $R(z) = z - z_0$ is the radius of curvature of the spherical wavefront at plane z and quantities with the index 0 represent quantities at the waist, i.e. the point of minimum size of the beam.
More generally, it is possible to find an expression of $u_n(x)$, which are the higher-order mode solutions of Eq.(1.3). Depending on what set of coordinates we used to describe the transverse plane, it is obtained a proportionality to Hermite polynomial solutions, or the Laguerre ones. They both represent a base in which to describe a paraxial beam (for a fully satisfying mathematical explanation see [3]):

$$E(x,y,z) = \sum_n \sum_m c_{nm} u_n(x,z) u_m(y,z) e^{-ikz} \tag{1.5}$$

In Fig.(1.1) are shown some examples of these modes:

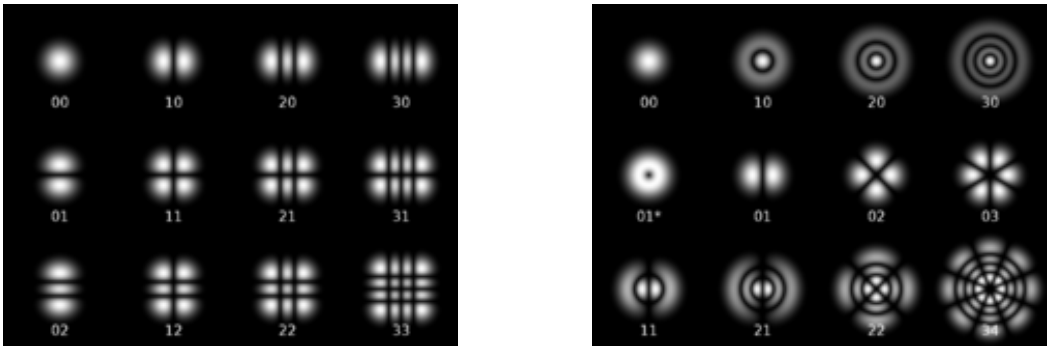

(a) Hermite-Gaussian modes

(b) Laguerre-Gaussian modes

Figure 1.1: Spatial modes of a laser beam inside a cavity

These eigenmodes will resonate at different frequencies, because of the *Gouy phase shift*: a phase shift associated with any wave passing through a focus, which depends on the indices of the mode.
So, let us describe more precisely what it means for a beam to be matched to a cavity.

A cavity defines a certain fundamental mode and all the higher-order ones are defined based on the fundamental. In other words, the cavity defines size and the position of the waist (ω_0 and z_0) of a gaussian beam inside of it and these parameters fully characterise every mode.
On the other hand, a beam incident on a cavity can be described with one of the basis described above, determined by the cavity itself; so, if the frequency of the beam correspond to one of the resonant frequency of one of these modes, that component of the incident beam will resonate and all the others will be reflected.

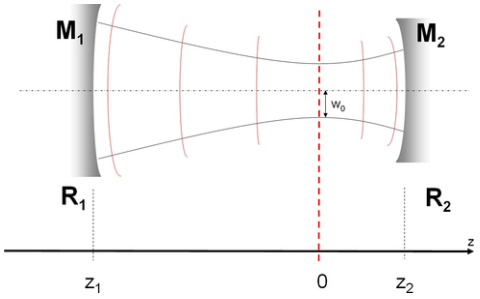

Figure 1.2: Reflection of a beam inside a cavity

Beams purely consisting of gaussian mode are usually preferred in optical experiments because of their relative simplicity to be described and manipulated.
The procedure of shaping an optical beam such that it is only composed of one specific mode defined by a cavity (usually the fundamental) is called *Mode Matching*.
Suppose to have a certain optical cavity, that defines a gaussian resonant mode with given parameters w_0 and z_0, and an incoming gaussian beam with different parameters that you want to match to the cavity. To do so, we can use lenses to create a beam that will match the 00-eigenmode of your cavity, becoming spatially matched; when also matching the resonant frequency of the gaussian mode, it will resonate in the cavity while any other residual mode still present will be reflected and lost.
With a well matched input beam it is possible to limit, and nearly eliminate, power losses due to the presence of some mismatched modes.

To predict how a laser will be influenced by the presence of a lens, the *ABCD-matrix* technique can be used.
We can thus calculate which optical elements we should use to obtain a specific final beam and, also, where to position them; it is sufficient to know the characteristics (waist size and position) of the initial and final beam.
It is possible to associate at every optical element, such as a lens or empty space, a specific 2×2 matrix. The multiplication of the matrices representing all the optical elements (including free space) traversed by the beam will give the linear application that will transform the initial beam in the final. Before doing this, we need to define the complex reduced radius of curvature of a beam $\hat{q}$:

$$\frac{1}{\hat{q}} = \frac{n}{q} = \frac{1}{\hat{R}} - i\frac{\lambda_0}{\pi\omega^2} \qquad \hat{q} = z - iz_R \tag{1.6}$$

where q is the complex radius of curvature, n the refraction index of the medium, $\hat{R}$ the real reduced radius of curvature equal to R/n, i the imaginary unit, λ_0 the wave length in vacuum of the beam and ω the size of the beam, z the position on the propagation direction and z_R define the *Rayleigh distance*. R is the radius of curvature of the wavefront.
The transformation induced by the *ABCD-matrix* relates the complex reduced radius in two different points as follow:

$$\hat{q}_2 = \frac{A\hat{q}_1 + B}{C\hat{q}_1 + D} \tag{1.7}$$

where A, B, C, D are the components of the *ABCD-matrix* of the optical elements:

$$ABCD = \begin{bmatrix} A & B \\ C & D \end{bmatrix} \tag{1.8}$$

It is thus possible to know the features of a beam in every position of the optical path and to predict how it will be transformed by the passage through a combination of optical elements [3].

1.1.2 Thermal Adaptive Lensing

Even if a beam is matched to a cavity, by design, machining and positioning errors, as well as thermo-optic and thermo-elastic effects induced in the optical elements by absorbed laser power, will generally result in an imperfect matching.
Indeed, the heat coming from the incident beam, or some other external source, can cause shape deformations, governed by the coefficient of linear expansion (α_T), and spatially dependent refractive indices, depending on the thermo-refractive coefficient (dn/dT). This effect is modelled by the introduction of imaginary lenses at the surface, but the focal length of these lenses will change according to the geometry of the material and to the temperature profile on it. This phenomenon is called thermal lensing.
Depending on the values of α_T and dn/dT of different materials it is possible to obtain both diverging ($\alpha_T > 0$, $dn/dT > 0$) and converging lenses ($\alpha_T < 0$, $dn/dT < 0$) [5, 6]. This effect is inevitable on the optical elements of an interferometer, but it can, also, be used on purpose to create a device, named adaptive optical element (AOE), with a controlled heat geometry, designed to contrast the effect on the other elements, as shown in Fig.(1.3).

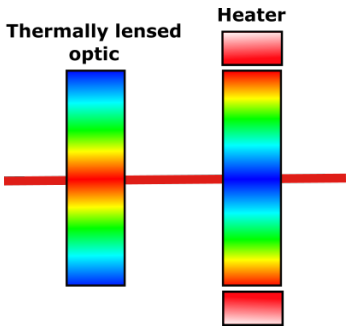

Figure 1.3: Example of an *AOE* applying an opposite thermal gradient and the main lens heated by the passage of the laser beam

Similar devices are already employed in *LIGO* to compensate part of the thermal deformations on the main mirrors, but they are very complex, big and hard to install.
Two ways of heating the *AOE* are usually used. The first consist of a system of addictional lasers that heat the *AOE* in the desired areas, to create the right thermal gradient (this is the one currently employed in *LIGO*, which uses a system of CO_2 lasers). The second and more simple way is to use external heaters attached on the barrel of the optic, that can provide indipendently heat[4, 5, 6].
The latter is the one that we will use during this thesis.

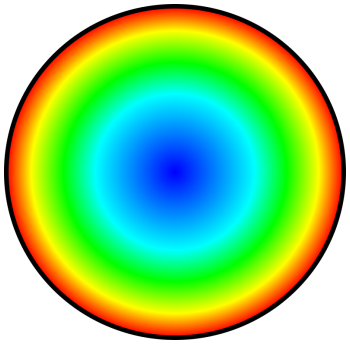

Figure 1.4: Example of a circular gradient on a *AOE* obtained using external heaters on the barrel

Our device is built with four independent heaters, in order to have four independent quadrants on the lens. This configuration allow to control the astigmatic and steering effects on the beam, but these lie outside the purpose of this thesis. We will only concentrate on obtaining a circularly symmetric thermal gradient, to control only the focal length of the *AOE*.

In a *AOE* as described above, receiving an heat flux from a set of heaters lying onto

its barrel, the thermal diffusion equation describing the temperature distribution is:

$$\rho C \frac{\partial T}{\partial t} = k\nabla^2 T + Q \tag{1.9}$$

where ρ is the density of the material (kgm^{-3}), C is the specific heat ($Jkg^{-1}K^{-1}$), $T(t, r, z, \phi)$ is the temperature depending on the radial coordinate r, on the angular coordinate ϕ, on the axial coordinate z and on the time t (Fig.(1.5)); k is the thermal conductivity ($Wm^{-1}K^{-1}$), ∇ is the gradient operator and Q is the heat generated per unit of volume in the optical element (Wm^{-3}).

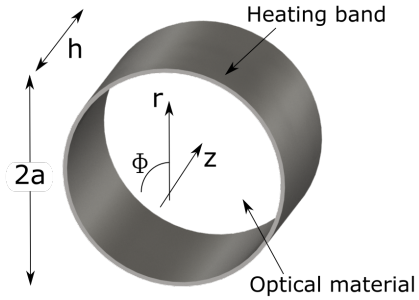

Figure 1.5: Coordinates and measures definitions for the considered problem

Eq.(1.9) describes both the transient solutions and the steady state, but for simplicity we will consider only the last ones, resulting from:

$$k\nabla^2 T + Q = 0 \tag{1.10}$$

In addition to Q there will be a heat flux through the surfaces of the AOE, which can be divided in two parts: q_{rad}, which is the flux radiated back into the surroundings; q_{ext}, which is the known flux supplied by the external heaters.
q_{rad} will follow the *Stephan-Boltzmann* law as follows:

$$q_{rad} = \epsilon\sigma(T^4 - T_{amb}^4) \tag{1.11}$$

where σ is the $Stephan - Boltzmann$ constant ($5.67 \times 10^{-8} Wm^{-2}k^{-4}$), ϵ is the emissivity of the material and T_{amb} is the ambient temperature.
Reminding these relations and applying three boundary conditions coming from the known informations of the heat input from the heaters, it is possible to come to an expression for the temperature profile. We can simplify the solution considerably by assuming that the temperature depends only on the radial coordinate from the center of the lens and ignoring the dependence in the axial direction.
The temperature distribution of a cylinder under constant heat load at the barrel is [4]:

$$T(r) = q_{ext}\frac{a^2}{4k}\left(\frac{r^2}{a^2} - 1\right) + T_0 \tag{1.12}$$

where T_0 is the temperature in the center of the optic and a its radius.
As stated in Eq.(1.12), the temperature dependence on the radius introduces a gradient through the *AOE*, which will induce a lens-like profile thanks to thermal expansion and the temperature dependence of the refractive index. The power of this lens depends on the thermo-optic and thermo-mechanical properties of the material and, it is possible to describe the focal length f of the *AOE* as follows [4]:

$$f = \frac{-4k}{h\left[\frac{dn}{dT} + \alpha_T(1+\upsilon) \times (n-1)\right]} \frac{1}{q_{ext}} \tag{1.13}$$

where υ is *Poisson's ratio*, n is the refractive index of the material, α_T is the coefficient of thermal expansion, dn/dT is the thermo-optic coefficient and h is the height of the barrel. From Eq.(1.13) we can define the so-called *Figure of Merit*, or *FOM*, representing the strength of the lens produced for a given geometry, incident heat flux and material. So, it represents an easy way to compare optical materials and its expression is:

$$FOM = \frac{\left[\frac{dn}{dT} + \alpha_T(1+\upsilon) \times (n-1)\right]}{k} \tag{1.14}$$

Comparing different materials, *SF57* rises to be the most suitable for the application in *Thermal Lensing*, since it has $FOM = 25.1\mu m/W$. fused silica, for example has only $FOM = 6.3\mu m/W$.
Abandoning the circular symmetry of this model, it is possible to achieve and control astigmatic and deflective effects with an *AOE* employing four separate heaters for the four quadrants. By changing the heat independently on the heaters it is possible to obtain astigmatic effects by "stretching" the thermal gradient along one of the two axis, maintaining the central symmetry of the gradient. While, abandoning even the central symmetry results in thermal beam steering, which can be used to perfectly align the laser to a cavity [6]. The results achieved at *UF* with *Thermal Lensing* will be discussed in the following chapters, but for now it is sufficient to know that the model given by these equations above is in good agreement with the experimental situation considered.

1.2 Gravitational Waves

Gravitational waves are one of the most fascinating predictions of Einstein's *General Relativity*, that were directly observed for the first time on sept 2015 by the american interferometers *LIGO*. They are a transverse radiation that travel through space-time at the speed of light, perturbing it as they pass and carrying energy.
GW are the wave solution of linearized *Einstein* equations in vacuum, describing how matter affects the space-time curvature, and can be characterized by two independent polarizations: "+" (plus) and "×" (cross). Their effect on a physical object is to, alternatively, stretch and shrink distances along two perpendicular axis, inducing a relative length change. As the name suggest, the difference between "+" and "×" is that their axis have a angle of 45° between each other, as shown in Fig.(1.6)[1, 2].

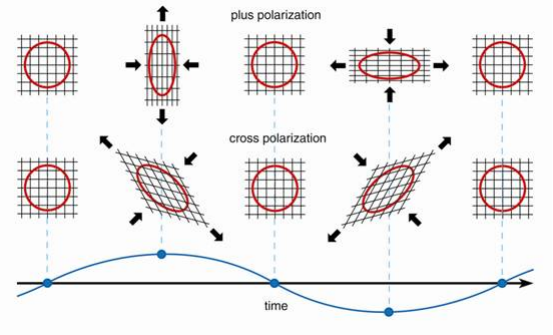

Figure 1.6: "+" and "×" polarizations acting on a spherical configuration of masses

The different nature of *EMW* and *GW* makes the latter interesting for the study of the inner matter of astronomical objects that, until now, has remained inscrutable. Also sources that do not emit *EMW* at all, such as black holes (exception made for some gamma burst and the radiations from the accretion disk around them), become "visible" with this new type of information. Furthermore, they can give us clues on the expansion history of the *Universe* and can possibly show us some new physics.
However, *GW* are extremely hard to observe, because the distorsion produced is extremelly small. Indeed, every mass distribuction changing its quadrupolar moment generates *GW*, but we need an extreme quantity of mass and acceleration to make these waves measurable [1, 2].
For this reason, one of the most suitable source is a system of merging compact and massive astronomical objects. Of our particular interest systems of merging neutron stars, that can give us information both via *EMW* and *GW* [10].

1.2.1 Detection of Gravitational Waves

GW carry energy, but even if the source is an extremely strong and violent event happening in our own galaxy, the amplitude of the associated space-time distortion is extremely small and difficult to detect. For example, the enormous amount of energy emitted by the first observed event of a binary black hole merger, occurring about 1.3 billion of light years away, was equal to 3.0 ± 0.5 solar masses ($\approx 5 \times 10^{47} J$), but the peak amplitude of the signal that reached us was only of $\frac{\delta l}{l_0} \approx 10^{-21}$ [8], where l_0 is the length at rest of the interferometer arm cavities and δl its change.

So, how could we possibly measure something so tiny?
Since 1960s *GW* detectors of different types have been built and constantly improved; these are two of the most important types of detectors:

- ***Weber bars*** are conceptually very simple devices that consist of a large and solid metal bar isolated from any outside vibration. An incident *GW* excite the bar's resonant frequency, so that it should enhance the amplitude of the signal to detectable

values. These bars are often cryogenically cooled to temperature in the order of the mK and can be of different shape. Some honourable mentions are the spherical *MiniGRAIL* detector and the italian ultracryogenic resonant bar *AURIGA*.
However, these detectors have limited sensitivity and a very narrow-band response.

- ***Interferometers*** are a more sensitive type of detectors that uses laser interferometry to measure the separation between two suspended test masses (which behave as if they were free falling in the direction and frequency band relevant for the measurement). Exploiting the difference in the phase of two lasers going in two orthogonal arms of the interferometer, it is possible to measure the strain caused by a passing *GW*. Some of the most important examples are the *LIGO* (**L**aser **I**nterferometer **G**ravitational-Wave **O**bservatory) interferometers and their italian counterpart *VIRGO*, that have already proven to be able to detect GW with the observation of six binary black holes merger and a binary neutron star merger. There is also an ongoing project of an interferometer orbiting the sun next to the Earth, the so-called *LISA* (**L**aser **I**nterferometer **S**pace **A**ntenna) interferometer. It consists of three identical satellites separated by a distance of $2.5 \times 10^9 m$, that is planned to be operative for 2034 and will be able to see low frequency GW signals [11].

1.3 *LIGO*

The american *LIGO* project consists of two twin interferometers both located in the United State of America and separated by a light travel time of $\approx 10ms$. Precisely they are in Hanford, Washington and in Livingston, Louisiana.

1.3.1 Operating principles and layout

LIGO is actually in his third configuration called *Advanced LIGO*, that has allowed the best sensitivity to go down to $\approx 5 \times 10^{-22} Hz^{-1/2}$. Its main elements are shown in Fig.(1.7). As we can see, it differs from a simple L-shaped Michelson-Morley interferometer for several additional parts; the most relevant feature for this thesis is that *LIGO* consists of a total of seven optical cavities:

- Input Mode Cleaner
- Power Recycling Cavity
- X and Y Arm Cavities
- Signal Recycling Cavity
- Output Mode Cleaner
- Squeezer

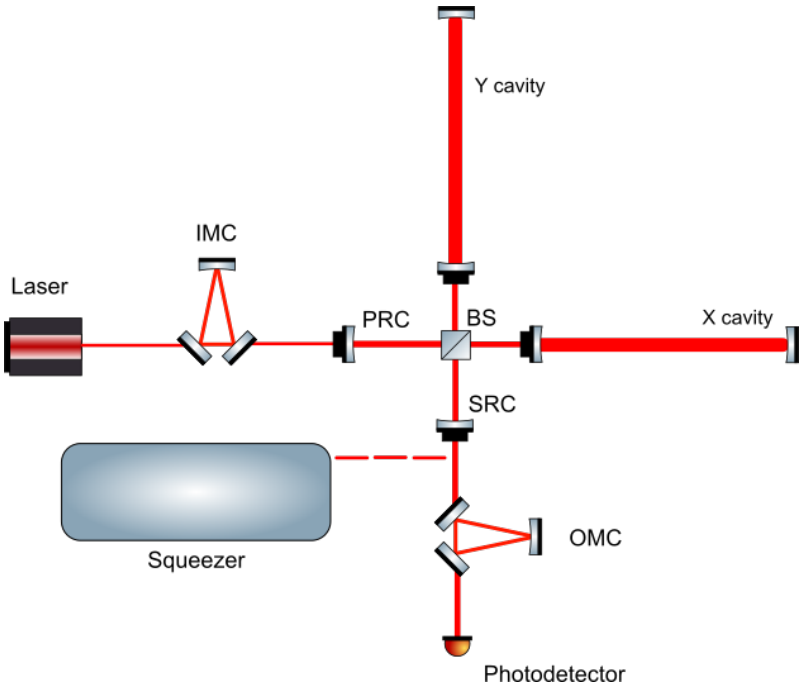

Figure 1.7: *LIGO* configuration plus the squeezed light source: IMC = Input Mode Cleaner, PRC = Power Recycling Cavity, SRC = Signal Recycling Cavity, OMC = Output Mode Cleaner, Squeezer (part of the future upgrades discussed in Sec.(1.3.3))

LIGO uses these cavities to define and "clean" the fundamental mode, increase the stored power and resonantly extract the GW signal. From an input beam power of "only" $125W$, the *PRM* increases that value by a factor 17 up to $\approx 2.1kW$ and then in every arm the power reaches values of $\approx 830kW$ [16]. This aspect can be alternatively seen as a way to increase enormously the effective length of the arms; in fact, their length is limited by the curvature of the Earth and by engineering issues of building a tunnel too long, but by making the light to reflect multiple times we can assume to have a much longer effective arm.
Optical cavities also allow to clean the beam selecting a specific eigenmode suitable to the experiment (Sec.(1.1.1)).

1.3.2 LIGO Sensitivity Limits

The current sensitivity of *LIGO* is limited by different factors.

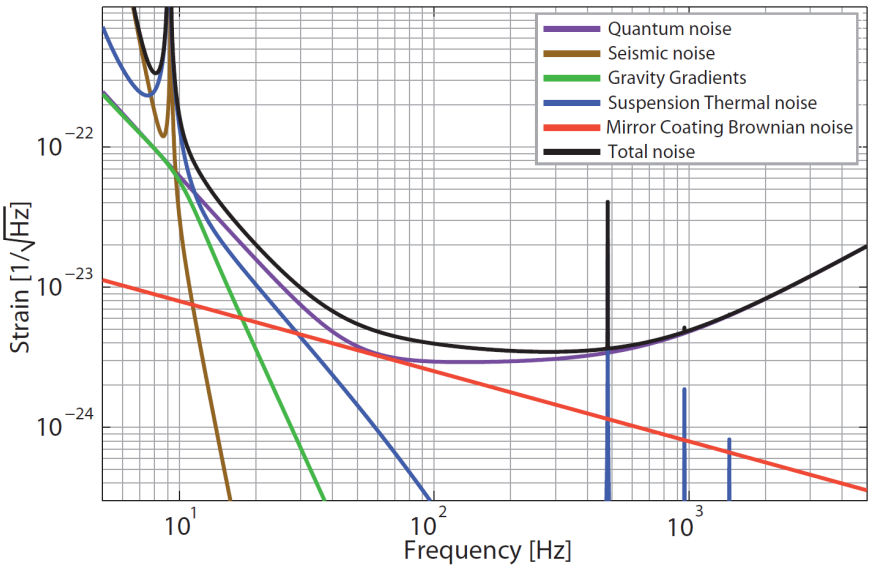

Figure 1.8: Curve of sensitivity of *LIGO* Livingston and Hanford

The principal sources of noise are:

- **Thermal Noise**
  The term "thermal noise" covers all noises sources that arise from thermal fluctuations of the atoms that make up the different components of *LIGO*. This includes the thermal noise from mirror coatings, surface and internal vibration modes of the test mass mirrors, thermal noise from the suspension wires and thermo-refractive noise through *ITM* transmission.

- **Quantum Noise**
  Quantum noise arises from the quantum nature of the electromagnetic field used to measure the position of the test masses. It manifests both in the measurement of the arrival time of the photons on the photodetector and in the pressure on the test masses caused by the photon momentum transfer on them while reflecting.

- **Seismic Noise**
  Seismic noise consists of all vibrations concerning the seismic ground motion. For this reason, usually these interferometers are built in sites with a low displacement spectral density of ground motion ($\approx 10^{-8} m/\sqrt{Hz}$ at $1Hz$ at the *LIGO* sites), but to minimize ulteriorly this noise, all the optical components inside *LIGO* are isolated through very complex mechanical suspensions, that actively and passively eliminate every external vibration on the devices.

- **Gravity Gradient Noise**
  Fluctuations in the gravitational field of the local environment can cause some displacement noise onto the test masses. This noise is caused by all moving mass bodies

around the interferometer, such as trains, cars, people, or by environment changes, such atmospheric pressure and subterranean sediment settlement.

- **Other Noise Sources**
  Other sources of noise are feedback control noise, electronic component noise, photothermal noise, residual gas and stray light.

The two noises that mostly limit the sensitivity of the modern detectors are the thermal and the quantum noises, so the upgrades that will be performed on *LIGO* are aimed to get rid of a part of their sources.

1.3.3 Quantum Noise and Squeezed Light

The electromagnetic field in the interferometer is characterized by amplitude and phase, which both have uncertainties at the quantum level and cause two different types of noise. Firstly, photons transferring their momentum onto an object will generate a force on that object, that causes mechanical motion. The uncertainty in the amplitude quadrature of the electromagnetic field, that translates into uncertainty in the photon number at a particular time/measurement point, will make this force to fluctuate, creating a noise proportional to the optical power. This causes the so-called Quantum Radiation Pressure Noise (*RPN*).
Secondly, the uncertainty on the arrival time of the photons to the measurement point causes the Photon Shot Noise (*PSN*); as the uncertainty in the phase quadrature increases with decreasing number of photons present, this noise is inversely proportional to the optical power.

$$\sigma_{total} = \sqrt{\sigma_{PSN}^2 + \sigma_{RPN}^2} \propto \sqrt{\left(\frac{1}{P_{opt}}\right)^2 + P_{opt}^2} \tag{1.1}$$

The proportionality of these two noises makes the *PSN* dominant at low power regime, while in high power regime *RPN* contribution will overcome the other. However, there is a point where they are equal and where the total quantum noise is at a minimum. This limit is known as *Standard Quantum Limit*, or *SQL*, shown in Fig.(1.9). Without applying quantum optical techniques such as squeezed states, it defines the minimum quantum noise achievable.
Talking about frequencies, *PSN* is mostly dominant in the high-band, while *RPN* in the low-band [14].

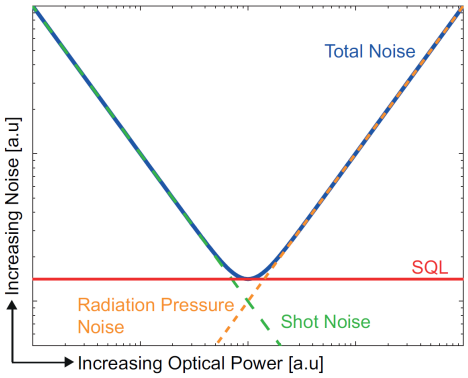

Figure 1.9: Quadrature sum of *RPN* and *PSN* showing the *SQL*

The phase and the amplitude of the signal are two non-commuting observables which have their uncertainties related by:

$$\Delta A \Delta \phi \geq 1 \tag{1.2}$$

Trying to diminish the uncertainty on the phase will enhance the one on the amplitude, and vice versa.
We then can consider the idea of "shaping" the uncertainties to reduce one of them, depending on which frequency band we want to investigate.
A full quantum-mechanical analysis of an interferometer shows that RPN and PSN don't depend on fluctuations on the laser beam entering the so called "symmetric port", which cancel out because of the common mode rejection of the interferometer, but rather come from fluctuations of the vacuum state entering the "anti-symmetric port" (the output port of a GW detector). We can imagine a state containing no photons on average as a state of the vacuum in which both the uncertainties are $\Delta A = \Delta \phi = \pm 1$. This is, obviously, a state of minimum uncertainty.
However, let us consider that we want to increase our sensitivity on the high-frequency band. Reminding that the uncertainty relation is multiplicative, we can push the uncertainty on the phase below 1 at the cost of increasing the other uncertainty, so that their product remains constant. Such a state of the vacuum is named *squeezed vacuum state* [13].

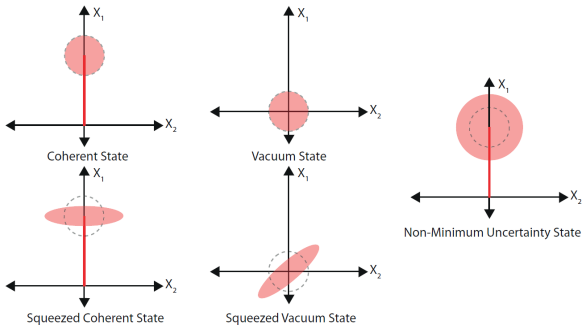

Figure 1.10: Different vacuum states represented as quantum phasor diagrams

The best method to decrease the quantum noise in an interferometer is to "inject" from the anti-symmetric port a squeezed vacuum state whose squeezing angle (the angle between the axis of the ellipse and the reference quadratures) depends on the frequency considered, so that, in the high-frequency band, it will diminish the uncertainty on the phase and, in the low-frequency band, on the amplitude. Such a state is called *frequency-dependent squeezed state*.
If some non-squeezed vacuum field (circularly shaped) enters in the optical path, it will sum up with the carefully prepared squeezed vacuum state, spoiling its characteristics. One of the main "ports" for this undesired vacuum are optical losses.

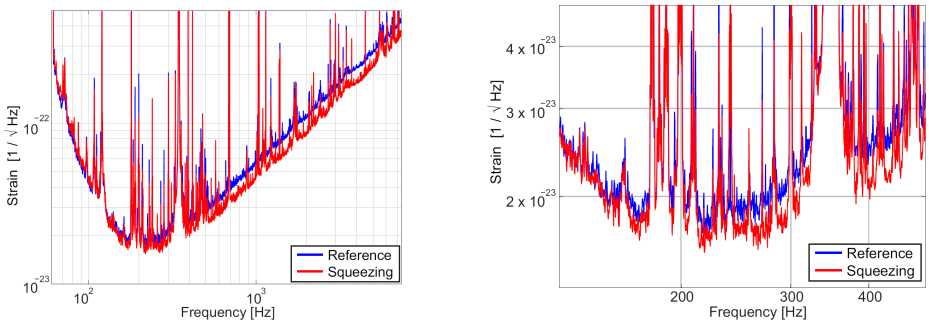

Figure 1.11: Comparison between the sensitivity curves of *LIGO* with and without the injection of squeezed light

Some squeezing experiment has already been run and it is proven that this technique will enhance the sensitivity of *LIGO* as shown in the Fig.(1.11) (squeezed vacuum state in phase direction) [7, 9].

Chapter 2

Previous Projects

The *LIGO* group at *UF* has been working for several years to the development of an adaptive optical element suitable for use in *LIGO*. In particular, we will briefly describe two different versions of the same idea, which I will call *Prototype 1* and *Prototype 2.0*. We will call my project *Prototype 2.1*, because it can be thought as an important upgrade of the 2.0 version.
All of these devices have to respect some strict requirements in order to be *LIGO*-compatible. For example, there is a very restricted list of allowed materials which can be used in the *LIGO* high-vacuum due to outgassing concerns. Furthermore, the *AOE* would have to fit in a already overcrowded working bench in *LIGO*, so it has to be very compact. In addition, it has to have an high thermal efficiency to minimize the heat necessary to make it work. Releasing too much heat on the actively isolated optical table, on which the AOE would be installed, can in fact compromise its performances.

2.1 Prototype 1

Prototype 1 was first built in 2010 to study the shaping of a beam by controlled thermal lensing [6] and was used again in 2013 to test a feedback control of optical beam spatial profiles [5].

2.1.1 Holders, Heaters and the Lens

The first prototype of *AOE* was realized using four heaters pressed against the barrel of a $1.0cm$ long by $2.5cm$ of diameter flat disk of *SF57 glass*, as shown in Fig.(2.1) [4]. This type of flint glass, produced by $Schott^{TM}$ (USA), has been choosen because of its large thermal expansion (α_T) and thermorefractive coefficients (dn/dT), which assure the device to have a wide range of achievable focal length thanks to its high value of *FOM* (Sec.(1.1.2)) [4, 5].
In particular, the values of the thermal expansion, thermo-refractive coefficients and *FOM* are:

$$\alpha_T = 9.2 \times 10^{-6} K^{-1} \qquad \frac{dn}{dT} = 6.8 \times 10^{-6} K^{-1} \qquad FOM = 25.1 \mu m/W \tag{2.1}$$

The optic and the heaters were kept in place by four components made of *Teflon* and metal, called holders, pressed onto the lens through a system of screws. They chose Teflon to insulate the heaters, to minimize heat losses and maximize efficiency. Heaters consisted of nichrome ($NiCr$) wires sealed in *Kapton* with a resistance of 25Ω, which was thermally connected to the barrel of the glass through a copper spacer. So, heaters and spacers were held in place by the pressure provided by the holders.

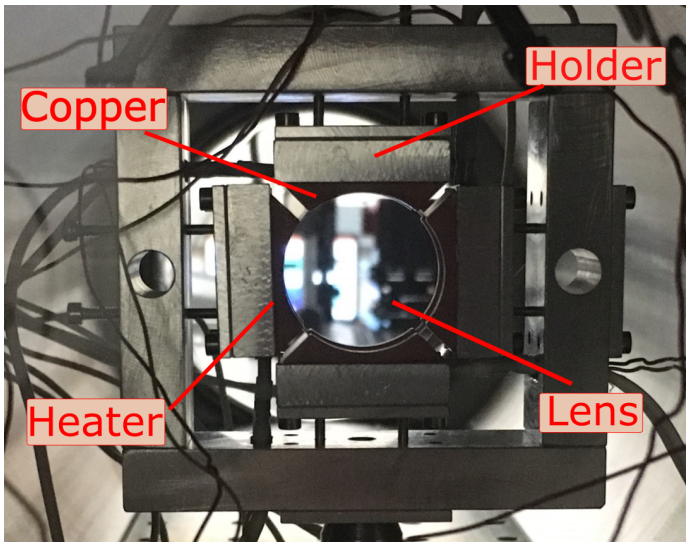

Figure 2.1: *Prototype 1* in a vacuum chamber used to minimize convection cooling effects

The system was also installed inside a vacuum chamber to simulate the operating conditions of *LIGO*, making radiation the dominant heat conduction mechanism, exception made for the conduction of heat through the structure of the prototype. The heaters were connected via standard copper wires, brought outside the chamber using electrical feedthroughs, to four independent power supplies. Each of them reaches a maximum voltage of $36V$ and a maximum current of $1.5A$.

2.1.2 Results and Issues

The range of power applied on every heaters was from 0 to $2.4W$, at which they reached the heater maximum allowed operating temperature of $200°C$ on the barrel of the lens.
A focal change in the range $-\infty$ to $-10m$ was obtained on both axis of the lens. It was also shown that beam quality and beam polarization were not affected by the usage of a *AOE* [4].
Then, with the experiment of 2013 they showed that it is possible to compensate time-dependent thermally induced aberrations of optics using an *AOE* in a feedback loop [5, 6].

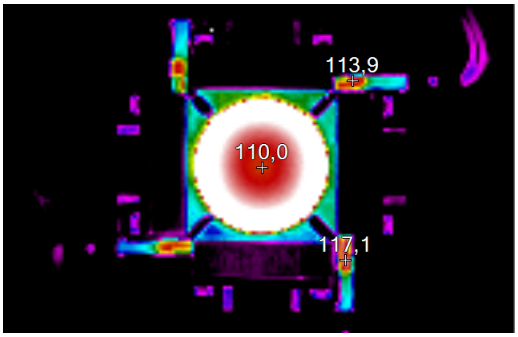

Figure 2.2: Thermal image of *Prototype 1* with three markers of temperature

In spite of these excellent achievements, the main issue of this configuration was the loss of a good amount of heat, diffused in the structure.
In order to evaluate the thermal efficiency of this device (we can see the temperature distribution in Fig.(2.2)), we compared the experimental data with the theory in Sec.(1.1.2). Eq.(1.13) describes the relation between the effective power on the lens and the focal length obtained, independently from the beam used for the experiment. Fig.(2.3) shows the theoretical focal length for 100% efficiency compared to the data of *Prototype 1*:

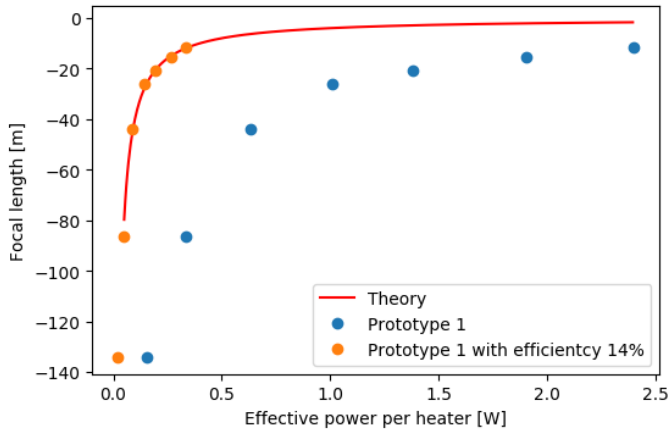

Figure 2.3: Comparison between the theoretical prediction for 100% efficiency and the experimental data from *Prototype 1* (orange points represent the efficient power per heater, whereas the blue ones the electrical power per heater). (Data from: *M. A. Arain, W. Z. Korth, L. F. Williams, R. M. Martin, G. Mueller, D. B. Tanner, D. H. Reitze, "Adaptive control of modal properties of optical beams using photothermal effects", Optics Express, (2010)*)

Since the experimental data were plotted versus the electrical power per heater (instead versus the effective one), we calculated their efficiency in order to make the data to match the theoretical prediction. The percentage obtained is 14% and it represents the thermal

efficiency of *Prototype 1*

2.2 Prototype 2.0

Prototype 2.0 was built in 2015 with the main purpose of solving the heat losses issue of the previous version, trying to obtain an higher efficiency. With a better insulated structure it would be possible to reduce the ratio of the heat lost through the structure to the heat employed to warm up the lens. This would mean that the *AOE* could provide the same lens with less power, previously wasted on the structure, increasing the thermal efficiency.

2.2.1 Heaters

The lens used was of the same kind as *Prototype 1*; instead they changed completely the heaters. As shown in Fig.(2.4), they decided to use a deposition of *NiCr* onto the barrel of the lens, instead of external heaters pressed onto it. To make them independent from each other, the deposition had four separation lines of $\approx 1mm$, visible as the slightly darker part on the barrel in Fig(2.4).

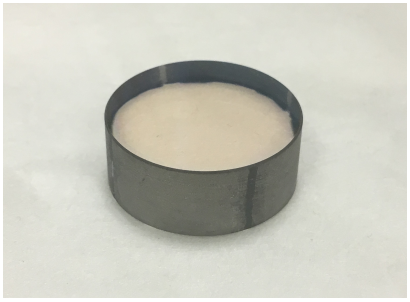

Figure 2.4: *SF57 glass* disk with the *NiCr* deposition used in *Prototype 2.0*

The layer of *NiCr* had a thickness of $\approx 3.7nm$ and each segment had a intrinsic resistance of $\approx 64\Omega$ [12]. The term intrinsic is used to distinguish between the resistance of the heater itself and the contact resistance, since we will see that the latter will play a main role in the performance of the device.
The deposition was performed using a *MicroEtch Machine*, showed in Fig.(2.5). The technique is called *sputtering* and uses ionized Ar atoms accelerated into a blueish beam towards a *NiCr* target; the whole system is inside a vacuum chamber, provided with a rough pump and a turbo pump to go down to $10^{-6} - 10^{-7}torr$. When an atom collides with the *NiCr* surface, it ejects *NiCr* molecules that will deposit onto everything standing on their path. The element to be coated is then mounted on a rotating support, to assure that the coating will be uniform.

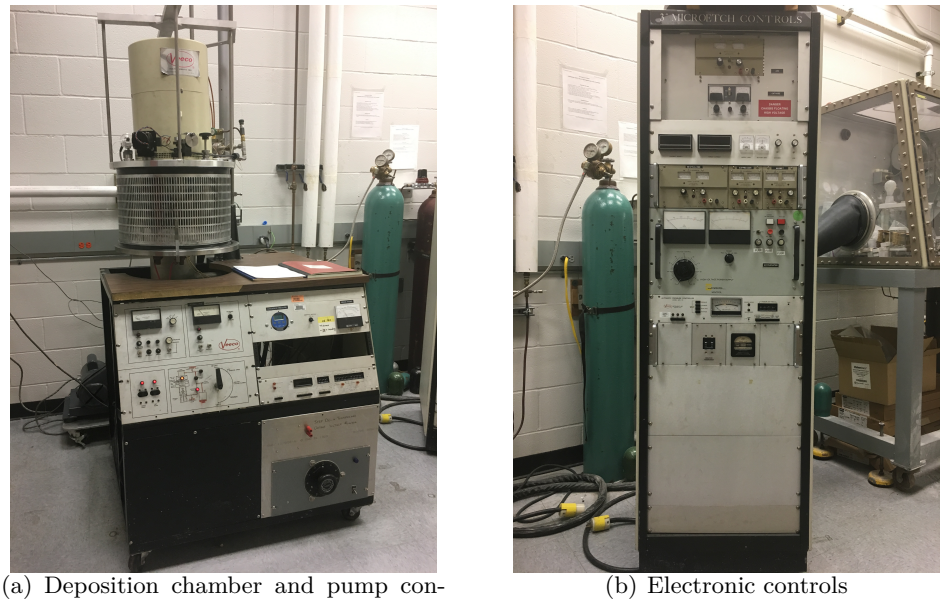

(a) Deposition chamber and pump controls

(b) Electronic controls

Figure 2.5: Complete setup of the *MicroEtch Machine*

The particular model of the machine, present in *UF* laboratories, allows to control the thickness of the deposition at the level of $10^{-10}m$, so on atomic scales.

2.2.2 Holders and their Positioning

Since the heaters were deposited onto the lens, the holders would have to provide electricity to them. For this reason, they were designed to have wires of copper wrapped around them, and making contact with the barrel, as shown in Fig.(2.7).
Holders were made of *Macor*, a glass-ceramic with excellent thermal properties (Sec.(3.1.2)). As we can see from Fig.(2.6), this version of the *AOE* had a system of springs and screws that provided the pressure to hold the lens. There were two screws for every holder to connect them to the external squared shaped support. Each of them had two nuts that allow to modify the position of the holder and a spring to provide the pressure to hold the lens in place.
Since it is not practical to have threads on *Macor* (as part of *LIGO* policy, threads on Macor can only be used once), a way to fix screws on the holder was designed; in other words, two holes correspondent to the position of the screws were machined and a little metallic part with threads was used to fix them (Fig.(2.7)).

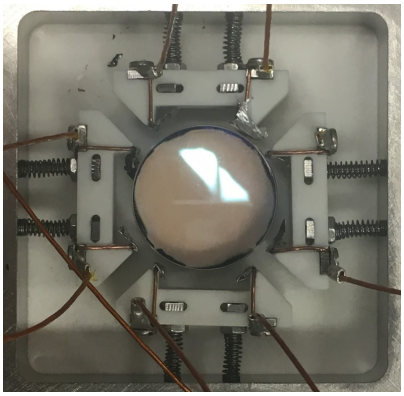

Figure 2.6: *Prototype 2.0* completely assembled

The mechanism to assemble the electrical wires, that would provide current to the heaters, was slightly more complex. Firstly, the external wires coming from the power supplies, had to be connected to the holder. This was made by another metallic part with threads, used to plug these wires on a couple of screws. These screws had a double function, in fact they were also used to clamp the electrical wires wrapped around the holder; these wires were long enough to have their terminations in the upper part, so that they could be clamped by the screws.

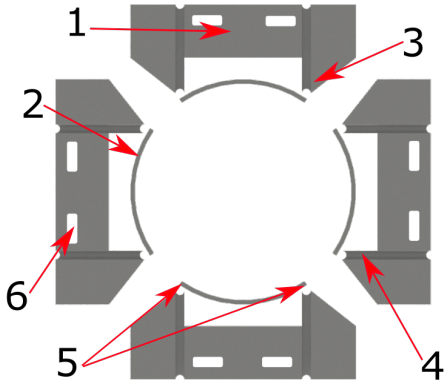

Figure 2.7: Geometry of the *Prototype 2.0* (not in scale with the real device). The main parts are labelled as follows: Holder (1), Heater (2), Triangular shaped part (3), Electrical wire guide (4), Contact pads (5), Metallic part with threads to fix the screw to the holder (6).

To sum up, the entire path of electricity was as follows: the heaters received electricity from the electrical wires on the triangular shaped parts of the holders; these wires were wrapped around the holders and received electricity from the external wires; they were both clamped by the two little screws on top of every holder, which made them solid with each other; finally the external wires were plugged into power supplies that act as source

of energy.
As we can see in the scheme in Fig.(2.7), every holder was positioned to provide electricity to a single heater, making contact at the two extremes, which will be called from now on *contact pads*. In this way, a holder had both + and − polarization of the current.

2.2.3 Issues

This version has several issues, mainly related to the imperfect mechanical contact between the electrical wires and the heaters. This causes a lot of difficulties in assembling the device, in particular in obtaining contact with all heaters at the same time. In other words, the contact resistance is very variable and sometimes even too high to let a sufficient current flow into the heaters. Assuming to have made contact simultaneously with all heaters, the effective resistance (equal to the sum of the intrinsic and the contact one) can vary from the ideal value of $\approx 64\Omega$ to $\approx 250\Omega$.
Another issue is represented by the mobility of the holders during the assemblage. In fact, the mechanism which supports them can be bent easily, making holders difficult to position. This causes even more complexity in assembling the device and, sometimes, causes the electrical wires of two adjacent heaters to be so near that the current would rather go through the separation lines, than into the heaters, as shown in Fig.(2.8). This behaviour is maybe due also to a non excellent deposition and the presence of a finite resistance between contact pads of two different heaters.
Moreover, it is difficult to obtain a perfectly straight wire at the end of the triangular shaped parts, due to the excessive hardness of the wires, resulting in reduced contact surface and increased the contact resistance.

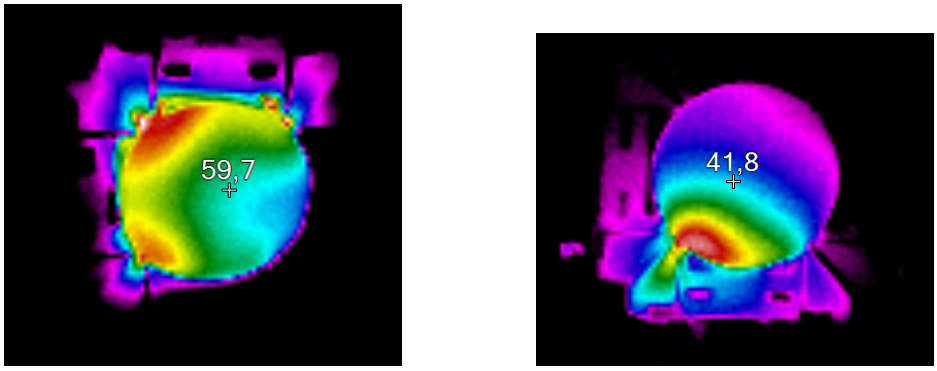

(a) (b)

Figure 2.8: Examples of thermal images of the *Prototype 2.0*, where current passes through the space between heaters

Because of the nearly overwhelming difficulty in assembling the *AOE* to achieve a good contact resistance, this version of the adaptive lens has never been tested in an actual focal length change experiment as *Prototype 1* [12].
Improving this device and making it a functional prototype was the main purpose of my

project.

Chapter 3

Prototype 2.1

Prototype 2.1, developed during this thesis, has some key difference with the previous one: an improved design and positioning of the holders, a new pattern and characteristics of the heaters and a new type of electrical wires. The main purpose of these changes is to make assembly easier and more reliable, while obtaining a low contact resistance between the electrical wires and the heaters, in order to diminish the effective resistance.

3.1 Holders and their Positioning

3.1.1 Design

For *Prototype 2.1*, we decided to change the geometry and the position of the holders and, in particular, how they were positioned in relations to the contact pads of every heater.
As we can see in the Fig.(2.7) and in Fig.(3.1), in *Prototype 2.0* every holder was connected to a single heater, providing on its own the potential difference necessary to make the current flow. In *Prototype 2.1*, every holder is attached on two different heaters near the separation line between them. An holder provides only positive or negative voltage. The holders shape itself implicates that now the distance between wires making contact with adjacent heaters is fixed by design and does not depend on the assembly procedure.
In addition, the new geometry ensures that the pressure provided by the springs will be nearly perpendicular to the contact pads, while previously it had a substantial shear component.
The system of screws and springs used to sustain and assemble all the structure and the mechanism to provide electricity has remained the same as the previous prototype. In this way, we were able to recycle the old parts for the purpose.

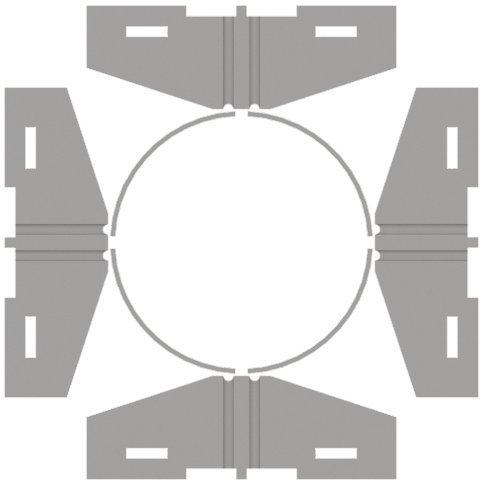

Figure 3.1: Geometry of the holders and the heaters

3.1.2 Material

We had two different possibilities for the choice of the material to use to machine holders: *PEEK* and Macor. We considered only these two materials, because Macor is the only one *LIGO*-approved for usage in ultra-high vacuum, whereas *PEEK* is used in *LIGO* for prototyping.

- *PEEK* (polyether ether ketone) is a organic thermoplastic polymer used in many engineering applications, in fact is one of the few plastics compatible with ultra-high vacuum. It has good mechanical properties and a fairly high melting point for a plastic material. In fact, it melts at $343°C$. Its maximum operating temperature is $250°C$.

- *Macor* is a white glass-ceramic. It has excellent thermal properties, in fact can resist at temperatures up to $1000°C$, it has a very low thermal expansion and it is a very good electric insulator. It is widely used in ultra-high vacuum applications.

	M.O.T.$[°C]$	**Max Temp.**$[°C]$	**C.E.** $[°C^{-1}]$	**Dielectric const.**
PEEK	250	343	$\sim 5 \times 10^{-5}$	~3
Macor	800	1000	$\sim 100 \times 10^{-7}$	~6

Table 3.1: Main mechanical, thermal and electric properties of *PEEK* and *Macor*, where **M.O.T.** stands for *Maximum Operating Temperature* and **C.E.** for *Coefficient of Expansion*

Considering the properties shown in Tab.(3.1), Macor is much better than *PEEK* for the application in our prototype. In fact, relying on the previous results, the lens, and so all the device, could easily reach the limit temperature of *PEEK* of $250°C$. However, *PEEK* is easier to machine and it was available in our laboratory at the *UF*. So for prototyping we decided to use *PEEK*, but we kept the design of the holders suitable for the production with Macor, so that the future prototypes can be made in that material.

3.2 New Heaters

As shown in Sec.(2.2.1), the previous prototype had the heaters directly deposited on the barrel of the lens according to a very simple pattern: a uniform layer of *NiCr* interrupted four times to create the separation between the heaters. Given the large aspect ratio of the heaters (short and wide), obtaining a high enough resistance for effective joule heating required to make the deposited layer very thin; in turns this made it very prone to scratched and other damages, worsening the problem of obtaining a good and reliable electrical contact with the holders. Instead, we created a more complex pattern replacing the uniform layer previously adopted, so as to increase the effective length and reduce the width of the heater; this allowed us to increase the thickness to about $1\mu m$, keeping the resistance around an ideal value of 25Ω.
Fig(3.2) shows the pattern unwrapped in a $2D$-plane.

Figure 3.2: *NiCr* pattern unwrapped in a $2D$-plane

To very good approximation, for weak lensing, the total effect on the beam going through the *AOE* can be calculated by evaluating the integral of the optical path along the direction of propagation, which is just proportional to the integral of the temperature. In addition, every non-uniformity in the heat released at the barrel will mitigate moving toward the center of the lens thanks to the heat diffusion in the glass.
So considering a single heater, the dimensions of every vertical, or horizontal, path was estimated so that the heat released integrated in the vertical direction (i.e. along the optical axis) would be approximately constant along the horizontal direction (i.e. around the barrel). To do this, we considered every path as shown in the Fig.(3.3).

Figure 3.3: Scheme of the vertical and horizontal paths; the contact pads are the first and the last path

Using the *Joule's first law*, which relates the heat produced by an electrical current in a resistance, it is possible to calculate the power absorbed per unit of length. *Joule's first law* states:

$$P = \frac{\Delta Q}{\Delta t} = Ri^2 \tag{3.1}$$

and dividing the last member by the length along the horizontal direction L_x, we obtain the heat per unit of time and unit of length on the horizontal axis:

$$\frac{\Delta Q}{\Delta t \Delta x} = \frac{Ri^2}{L_x} = \frac{\rho L i^2}{S L_x} \tag{3.2}$$

where ρ is the resistivity of *NiCr*, L is the length of the path considered and $S = thk \times x$ is the surface of the cross section, thk the thickness and x the width we want to find.
The vertical paths have their length on the horizontal direction equal to $L_x = x$; whereas, for the horizontal ones $L_x = L$. Imposing the paths to provide the same heat and using Eq.(3.2), we obtained the following equation, where the first member is the heat released by an horizontal section and the second by a vertical one:

$$\begin{aligned} \frac{\rho i^2}{thk \times x_H} &= \frac{\rho L i^2}{thk \times x_V^2} \\ \frac{1}{x_H} &= \frac{L}{x_V^2} \end{aligned} \tag{3.3}$$

where x_H and x_V are respectively the width of the horizontal and vertical paths. It follows a relation between the quantities we want to estimate:

$$x_V^2 = L x_H \tag{3.4}$$

We decided a width of $1.2mm$ for the horizontal paths, resulting in $3.0mm$ for the vertical ones and $3.25mm$ for the teeth (the value was chosen to make the pattern fit on the barrel). The pattern was designed so that the electrical wires of the holders would land exactly in the middle of the contact pads, to be sure to have enough space for some variation in the positioning of them.
To perform the deposition, we designed a mask, shown in the Fig.(3.4), in which the lens can be inserted. The mask was built by the *UF* machine shop.

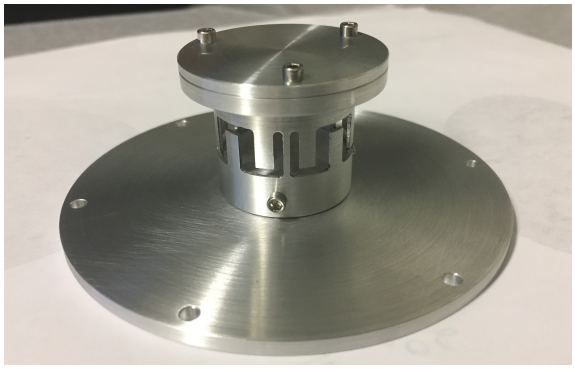

Figure 3.4: Mask used for the *NiCr* deposition

To protect the lens during the deposition, the mask was designed to leave a space of $0.5mm$ between the upper, and lower, surface and the beginning of the *NiCr* on the barrel. As an additional precaution, we applied on the surface of the optic a special commercial coating called *FirstContact*, routinely used in *LIGO* to protect the optics and leave them clean upon removal.
In order to obtain a precise deposition we needed to verify that the mean free path (*MFP*) of the *NiCr* molecules inside the vacuum chamber was bigger than the distance between the *NiCr* target and the mask. In fact, an eventual gap between the mask and the optic would have allowed to some *NiCr* molecule to deposit outside the defined path, spreading it. However, the condition stated before assures that the maximum angle at which they could travel under the mask was approximatively the ratio between the width of the path and the distance from the *NiCr* target (which was very small, considering the dimensions of the chamber and the paths).
So, we calculated the *MFP* from a reference value of pressure of $10^{-4}torr = 0.05Pa$ and a temperature of $325K$:

$$\lambda = \frac{k_b T}{\sqrt{2}\pi\sigma^2 P} \approx 1.12m \tag{3.5}$$

where σ is the *collision diameter*, that we have taken to be two times the radius of the *NiCr* molecule, considered spherical.
With a *MFP* this big, we surely were in the condition aforementioned.
The optic used is of the same type as in the previous prototypes. The final result of the deposition is shown in Fig.(3.5).

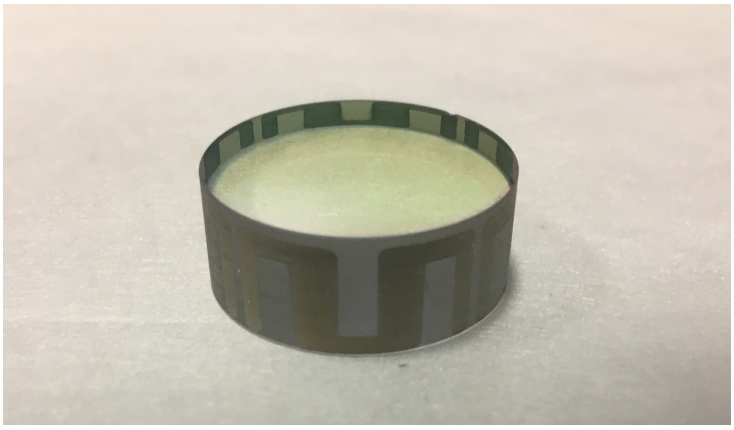

Figure 3.5: New lens with the *NiCr* pattern, slightly darker than the uncoated barrel

As it is clear from the Fig.(3.5), the lens was misaligned with the mask during the deposition, so the pattern is not perfectly centred on the barrel. In fact, due to some asymmetry in the machining of the mask or some bulge on the protective coating, the pattern has gone over the lower border. This alignment defect is not circularly symmetric so it will possibly cause some difference in the values of the resistance (it will be discussed in Sec.(4.1)). What prevented the lens from being coated was the additional protection given by the protective coating, that we applied on both sides.
The small chip visible in the upper-right corner of the picture in the upper-right part of the lens was a defect already present on the substrate, and is of little concern for our experiment.

3.3 Electrical Contacts

In the previous prototype the electrical wires, that carried electricity to the heaters, were made of copper. The hardness of copper could be a problem for the goodness of the electrical contact, because it would not easily deform following the contact pads surface irregularities; in addition, over repeated assembly attempts it could scratch the pads, degrading the quality of the electrical contact. To solve this issue we decided to employ a softer material wires.
One of the candidates was gold, due to its excellent thermal and electric properties and its softness, but it is very expensive and not very strong. So, instead of pure gold wires, we considered so-called *gold-filled* wires, that, in spite of the name, have the core made of a harder metal alloy and the surface made of gold (the thickness of the gold coating is about $5 - 20\%$ of the total radius).
Another candidate, considered only to test if the hardness played a main role in achieving a low contact resistance, was indium; this metal is very soft and cheap, but it melts already at $160°C$, making it unsuitable for use in the *AOE*.
In order to evaluate the impact of contact wire material on the quality of the electrical

contact, we run a very simple test: using one of the old holders and a test lens with our pattern, created to test if the *MicroEtch Machine* was correctly working, we measured several times the value of resistance that we could obtain by contacting a single heater with a holder equipped with wires of the three different materials. So, we assembled the holder with copper wires and we measured the resistance ≈ 20 times; then we repeated this procedure with the two other materials.

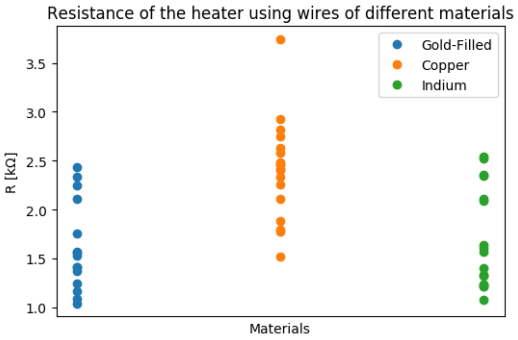

Figure 3.6: Values of resistance for different materials of the electrical wires.

The results of the test are shown in Fig(3.6): despite the large variability in the measured values, it is clear that indium and gold-filled wires have similar performance, and clearly better than copper. Since indium was never a true candidate for our experiment, we chose the gold-filled ones.

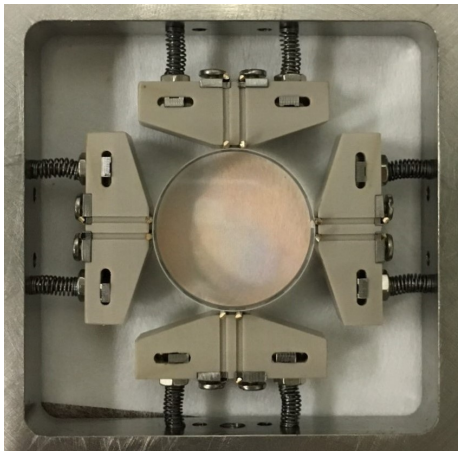

Figure 3.7: New prototype assembled with a test lens. Here the new holders, the terminations of the C-shaped gold-filled wires and the little screws, where the external electrical connections will be plugged, are clearly visible.

Not only the softness of the gold surface assured a good electrical contact with the heaters, but also the hardness of the inner alloy made it easier to clamp the wire on the holder. Indeed, it was so hard that was not necessary to wrap the wire all around the holder and clamp it with screws, as in the previous prototype, but it was sufficient a C-shaped piece to make it hold onto it. This greatly simplified the assembly process.
Fig.(3.7) shows the fully assembled prototype. Thanks to the new geometry and materials, *Prototype 2.1* was much easier to assemble than its predecessor, and it was easy to achieve values of resistance $\approx 20\Omega$.

Chapter 4

Testing and Data Analysis

4.1 Functional Tests

The device had to be tested to verify if the holders made contact with all the heaters at the same time, if the heaters had the expected resistance and how symmetric the thermal gradient was. Moreover, we had to confirm that the more of the electrical power was delivered to the lens and not dissipated through the holders as compared to *Prototype 1.0*. We used a small vacuum chamber, shown in Fig.(4.1), to test the device while simulating the operating conditions of *LIGO*.

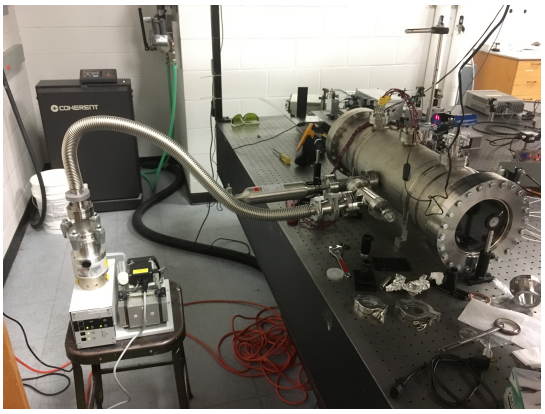

Figure 4.1: Vacuum chamber with the rough and turbo pump

However, we were not able to reach our target pressure, due to a problem with the vacuum system that we were not able to identify. The minimum pressure we could reach inside the chamber was $0.8mtorr = 0.11Pa$, which is at least 2 orders of magnitudes higher than what we wanted in order to make radiation the dominant heat conduction mechanism. We will take into account this aspect in the following discussions.

Firstly, we tested the resistances of the heaters connecting the external electrical wires

(regular copper electrical wires that can be plugged in a power supply, or a voltmeter) to the holders. The name convention for heaters and wires is as described in Fig.(4.2).

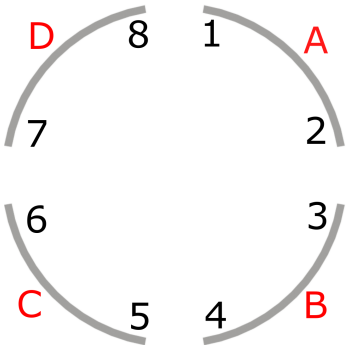

Figure 4.2: Scheme of heaters and electrical wires

These electrical wires were connected to four *TekPower 3645A* with a range of voltage $0 - 36V$ and of current $0 - 1.5A$ (the same used for the previous prototypes). Using them, we could measure the resistance dividing the voltage applied by the current flowing. Imposing the power on every heater to be $0.2W$, we obtained the following values of resistance:

	Vol.[V]	**Cur.[A]**	**Res.[Ω]**
A	1.960	0.10	19.6 ± 0.2
B	2.200	0.09	24.4 ± 0.2
C	2.200	0.10	20.2 ± 0.2
D	2.200	0.09	24.4 ± 0.2

Table 4.1: Test values of voltage and current to measure the resistance of the heaters (the error on V is $0.003V$; the error on the current is $0.01A$; the error on the resistance is calculated with the propagation of errors formula

These values are in good agreement with our goal resistance of approximatively 25Ω, the same used in *Prototype 1* (Sec.2.1.1).
To analyse the thermal gradient we used a thermal imager (*Fluke Ti10*); Fig.(4.3) shows the result:

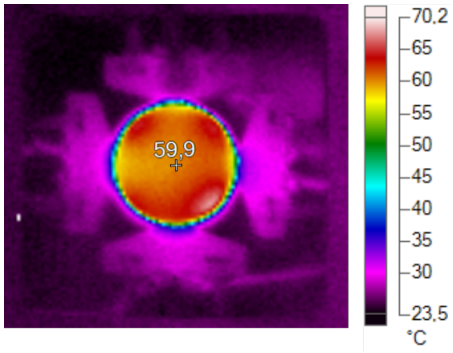

Figure 4.3: Test heating of the *AOE* to check the thermal gradient

As we can see in Fig.(4.3), the temperature seemed higher in proximity of heater "B". In order to verify if this was an issue with the heater itself (in Sec.(3.2) we mentioned the misalignment of the lens inside the mask used for the deposition, which could cause some non-symmetric defects), we rotated the lens of 90°, but after the rotation the temperature anomaly was still in the bottom-right position.
In addition, all the bottom part of the lens seemed slightly hotter than the top part. A possible explanation of these anomalies is the insufficient vacuum level inside the chamber, which did not completely prevent convection effects.
We also noticed that near the center of the lens it was not perfectly circularly symmetric as expected, maybe due to the issue stated before. These effects are clearly visible in Fig.(4.4), where the scale of temperature variations on the lens has been enhanced.

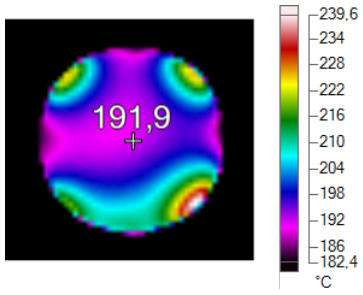

Figure 4.4: Enhanced image of the thermal gradient

These visible asymmetries could cause some astigmatic or deviating effect on the beam. However we had not time to investigate the issue and try to optimize the relative power of the various heaters to minimize the effect.
From this image it is also apparent that the heat flux seems to concentrate in the center of every heater, instead of being uniformly spread along the entire quadrant perimeter. This is simply explained by reminding that we are imaging the surface of the lens correspondent to the upper part of Fig.(3.3), while the heater pattern is optimized to deliver a circularly symmetric heat distribution when integrated along the optical axis. In fact,

it is not possible in our case to evaluate completely the symmetry of the thermal gradient using only our thermal images, because we can only analyse one of the two sides. Having at least the other would have allowed us to calculate the mean of the two images in order to get an idea of the real gradient. However, only one of the two windows of the vacuum chamber was transparent to *IR*, so we could not image both the surfaces.
Alternatively, verifying how well this target was met (and so how spherical the induced lens was) would have required to analyse the higher order aberration induced by the lens on the beam. However, this is a rather complex measurement that could not fit in the scope and time constrains of this thesis project.
Finally considering the temperature of the structure, we can see from Fig.(4.3), that it was severely diminished. Since the emissivity of *SF57* and *PEEK* are very similar (respectively $\epsilon = 0.92$ and $\epsilon = 0.95$), the image gives also an accurate idea of what temperature the holders reached.

We were satisfied of these preliminary tests on the *AOE*, so we set up an actual focal length change experiment. However, before talking about the experimental setup and data, we need to introduce a method to investigate the characteristics of a beam.

4.2 Beam Scan

A beam scan is a procedure used to estimate the position and the size of the waist of a gaussian beam (respectively z_0 and w_0; see Sec.(1.1.1)), which consists in measuring the transverse intensity profile of the beam in different positions on the propagation axis. Extracting the beam radius at each position is then possible to obtain w_0 and z_0 of the beam by fitting the data collected by the camera.
Indeed, Eq.(4.1) states that there is a hyperbolic relation between the squared radius of the beam and the position considered:

$$\omega^2 = \omega_0^2 \left(1 + \left(\frac{(z - z_0)\lambda}{\pi\omega_0^2}\right)^2\right) \tag{4.1}$$

So, it is possible to fit the data collected with:

$$\omega^2 = az^2 + bz + c \tag{4.2}$$

using the following relations between the coefficient of the parabola and the two parameters of the beam (ω_0 and z_0):

$$\begin{aligned} a &= \left(\frac{\lambda}{\pi\omega_0}\right)^2 \\ b &= -2z_0 \left(\frac{\lambda}{\pi\omega_0}\right)^2 \\ c &= w_0^2 + \left(\frac{\lambda z_0}{\pi\omega_0}\right)^2 \end{aligned} \tag{4.3}$$

The errors on these parameters are given by the covariance matrix function of the Python package *scipy.optimize.curve_fit* used to fit the data.
The errors on ω_0 and z_0 can be calculated from those on the parabolic parameters by the propagation of errors formula:

$$\begin{aligned} y &= f(x_1, x_2, ..., x_N) \\ \sigma_y &= \sqrt{\sum_{i=1}^{N} \sigma_i^2 \left(\frac{\partial f}{\partial x_i}\right)^2} \end{aligned} \tag{4.4}$$

with the obvious meaning of x_i and σ_i. In our particular case, it yields:

$$\begin{aligned} \sigma_{\omega_0} &= \frac{\sqrt{2}}{2}\frac{\lambda}{\pi}\sigma_a a^{-3/2} \\ \sigma_{z_0} &= \sqrt{\sigma_b^2 \left[\frac{1}{2}\left(\frac{\pi\omega_0}{\lambda}\right)^2\right]^2 + \sigma_{\omega_0}^2 \left[b\omega_0 \left(\frac{\pi}{\lambda}\right)^2\right]^2} \end{aligned} \tag{4.5}$$

Finally, the *Rayleigh distance* is defined as:

$$z_R = \frac{\pi\omega_0^2}{\lambda} \tag{4.6}$$

where λ is the wavelength of the laser. It represents the distance beyond which the relation between the radius of curvature of the beam and the position z becomes nearly linear; a beam scan is considered good to represent the behaviour of the beam if it covers at least 2 *Rayleigh distances* around the waist, so as to explore both the gaussian and linear parts of the beam [3].

4.3 Optical Path and Setup

To measure the focal power of the AOE as a function of electrical power, we used the simple optical setup shown in Fig.(4.5):

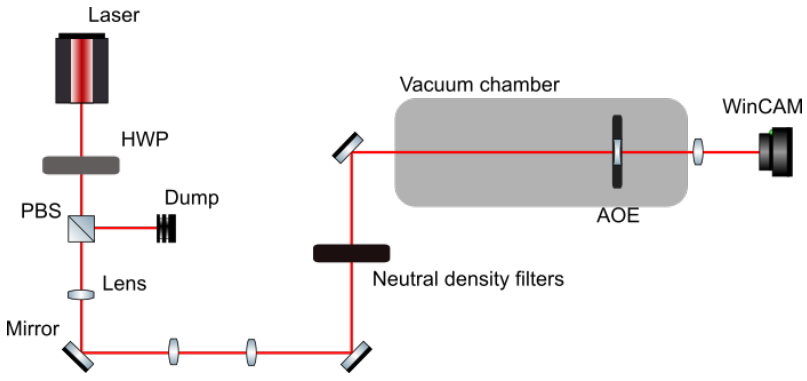

Figure 4.5: Scheme of the experimental setup

The polarizing beam splitter together with the half wave plate were used to adjust the power of the transmitted beam in a continuous fashion; on the other hand, to modify the power over a wider range of values, although in a discrete fashion, we used neutral density filters of various magnitude. This was necessary to optimize the power on the *CCD* of the *WinCAM* and avoid to saturate it, which would result in a distorted image.
The mirrors were used to route and align the beam inside the chamber and through the *AOE*; the lenses before the chamber where used to collimate the beam so that it would not diverge too much. A fourth lens positioned after the vacuum chamber, was used to obtain a beam with a small ω_0, in order be able to measure the beam over a range comparable to the Rayleigh distance within the available space on the table.
After all these components, we fixed a ruler on the workbench used both as a guide for the *WinCAM* and to measure its position.

4.4 Beam Scans

Figure 4.6 show an initial beam scan to register the characteristics of the initial beam, with the *AOE* switched off:

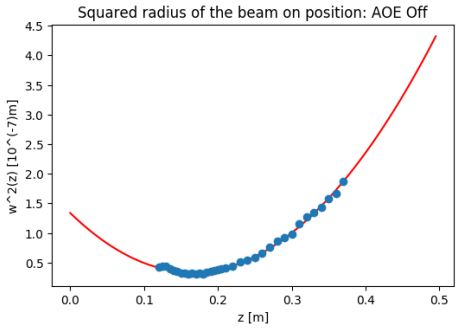

Figure 4.6: Beam scan with the *AOE* switched off (experimental data are shown as blue points, the red line represents the fit)

The resulting values of ω_0 and z_0 calculated with Eq.(4.1-4.3) are:

$$\omega_0 = (177 \pm 3)\mu m \qquad z_0 = (16.5 \pm 0.9)cm \tag{4.7}$$

We scanned a total length of $\approx 24cm$.
The *Rayleigh distance* calculated with the considered ω_0 is:

$$z_R = \frac{\pi\omega_0^2}{\lambda} = (9.3 \pm 0.3)cm \tag{4.8}$$

Since $24cm$ are ≈ 2.6 times greater than the *Rayleigh distance*, it should be sufficient to assure a good amount of data.

After taking the data for the initial beam, we begun the procedure to measure it at different values of power given to the heaters, using the condition to have the same power on every heater.
Tables (4.2-4.4) show the settings of voltage and current used for the measurements (the errors on voltage and current follows the rules explained in Tab.(4.1)):

(a) I measure at $0.12W$

	Vol.[V]	**Cur.[A]**	**Res.[Ω]**
A	1.480	0.08	18.5 ± 0.2
B	1.670	0.07	23.9 ± 0.2
C	1.670	0.07	23.9 ± 0.2
D	1.650	0.07	23.6 ± 0.2

(b) II measure at $0.38W$

	Vol.[V]	**Cur.[A]**	**Res.[Ω]**
A	2.670	0.14	19.1 ± 0.2
B	3.160	0.12	26.3 ± 0.3
C	2.770	0.13	21.3 ± 0.2
D	2.910	0.13	22.4 ± 0.2

Table 4.2: I and II measurements of the beam

(a) III measure at $0.50W$

	Vol.[V]	**Cur.[A]**	**Res.[Ω]**
A	3.110	0.16	19.4 ± 0.2
B	3.600	0.14	25.7 ± 0.3
C	3.140	0.16	19.6 ± 0.2
D	3.330	0.15	22.2 ± 0.2

(b) IV measure at $0.70W$

	Vol.[V]	**Cur.[A]**	**Res.[Ω]**
A	3.660	0.19	22.9 ± 0.2
B	4.35	0.16	27.2 ± 0.3
C	3.690	0.19	19.4 ± 0.2
D	3.900	0.18	21.7 ± 0.2

Table 4.3: III and IV measurements of the beam

(a) V measure at $0.93W$

	Vol.[V]	**Cur.[A]**	**Res.[Ω]**
A	4.21	0.22	19.1 ± 0.2
B	4.89	0.19	25.7 ± 0.3
C	4.22	0.22	19.1 ± 0.2
D	4.44	0.21	21.1 ± 0.2

(b) VI measure at $1.29W$

	Vol.[V]	**Cur.[A]**	**Res.[Ω]**
A	4.96	0.26	19.1 ± 0.2
B	5.84	0.22	26.5 ± 0.3
C	4.97	0.26	19.1 ± 0.2
D	5.27	0.25	21.1 ± 0.2

Table 4.4: V and VI measurements of the beam

The corresponding data, fits and thermal images are shown in Fig.(4.7(a)-4.12(b)).

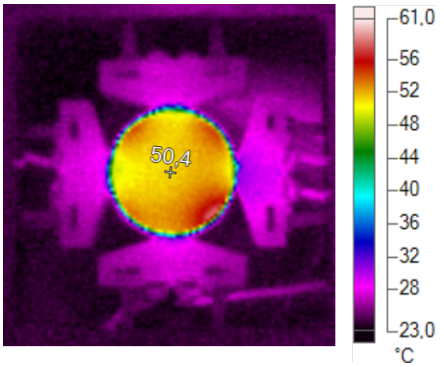

(a) Thermal image at $0.12W$

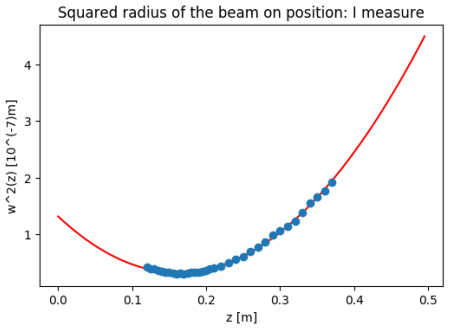

(b) Beam scan at $0.12W$

Figure 4.7: Thermal image and beam scan of the $0.12W$ configuration

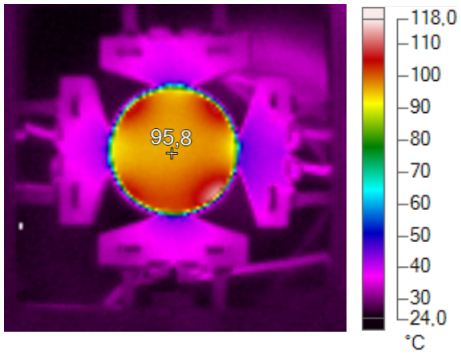

(a) Thermal image at $0.38W$

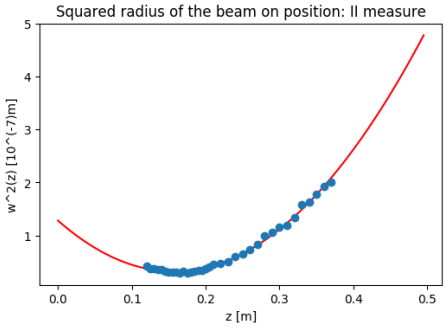

(b) Beam scan at $0.38W$

Figure 4.8: Thermal image and beam scan of the $0.38W$ configuration

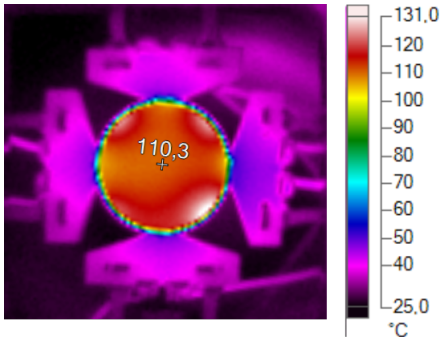

(a) Thermal image at $0.50W$

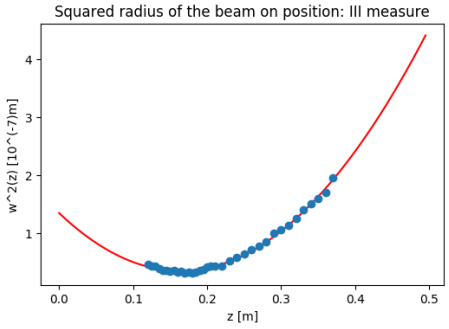

(b) Beam scan at $0.50W$

Figure 4.9: Thermal image and beam scan of the $0.50W$ configuration

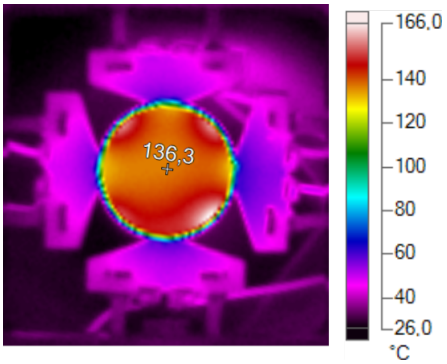

(a) Thermal image at $0.70W$

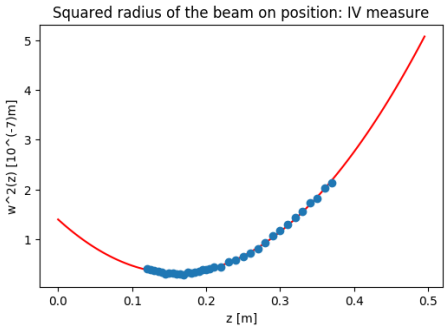

(b) Beam scan at $0.70W$

Figure 4.10: Thermal image and beam scan of the $0.70W$ configuration

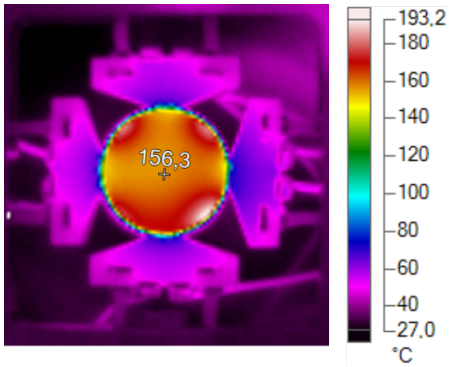

(a) Thermal image at $0.93W$

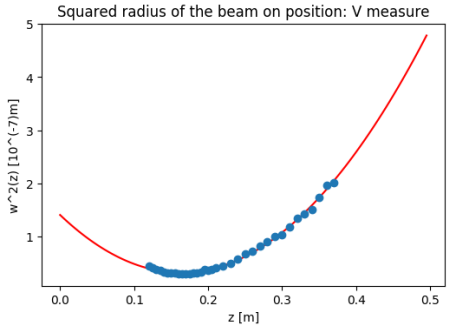

(b) Beam scan at $0.93W$

Figure 4.11: Thermal image and beam scan of the $0.93W$ configuration

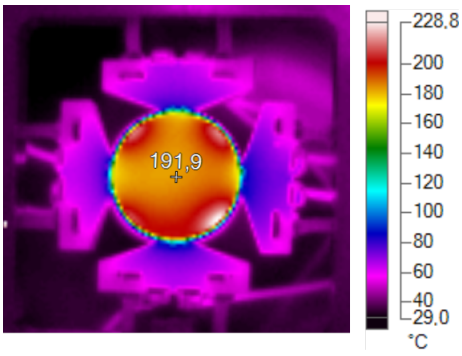

(a) Thermal image at $1.29W$

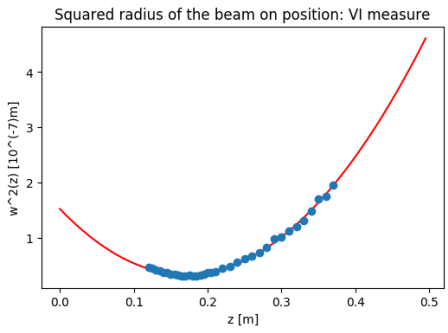

(b) Beam scan at $1.29W$

Figure 4.12: Thermal image and beam scan of the $1.29W$ configuration

We decided to stop at $1.29W$, because the AOE reached $250°C$ on the hottest parts of the

lens. Going further would have meant to exceed the maximum operating temperature of *PEEK*.

4.5 Results

The position and the dimension of the waist of the beam are calculated for every value of power provided to the heaters; using Eq.(4.1 - 4.3) and the data shown in Fig.(4.7(b) - 4.12(b)). The results are summarized in Tab.(4.5) and Fig.(4.13).

# Measure	$\omega_0^i[\mu m]$	$z_0^i[cm]$
I	174 ± 2	16.2 ± 0.6
II	172 ± 4	15.7 ± 1.0
III	176 ± 4	16.4 ± 0.9
IV	165 ± 2	16.0 ± 0.6
V	168 ± 3	16.4 ± 0.9
VI	168 ± 3	17.1 ± 0.8

Table 4.5: ω_0 and z_0 in the different configurations

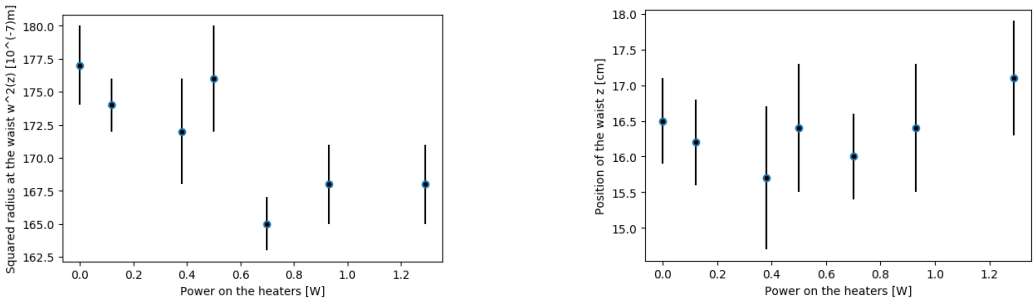

(a) ω_0 versus electrical power per heater

(b) z_0 versus electrical power per heater

Figure 4.13: Plots of ω_0 and z_0 on the power given to the heaters, where the first data is the initial beam with the *AOE* switched off

As we can see from Fig.(4.13), the behaviour of ω_0 and z_0 appears very noisy and do not points out a clear trend.
This behaviour is due to the size of the beam at the *AOE*. In fact, our target size was $\approx 2mm$, as in the experiments of *Prototype 1* [4, 5], but we obtained $\approx 250\mu m$. Such a small beam size makes it difficult to measure the effect of the thermal lens. Unfortunately, due to some technical difficulties and lack of time, we could not analyse the data during data taking, and we only realized the issue when we no longer had access to the experiment. We will see that, despite their low quality, our data still point to a substantial improvement in the performance of our device compare to *Prototype 2.1*. It is also impossible now to track back what exactly is the origin of this error, but probably it was a mispositioned

lens, which made the beam to converge too much.
To compare our data with the theory, we can calculate the expected focal power f of the *AOE* using Eq.(1.13) and assuming q_{ext} to be the full electrical power provided (100% efficiency). Then, using the *ABCD-matrix* technique explained in Sec.(1.1.1), we can obtain the expected change in the parameters of the beam passing the *AOE*. For the *Rayleigh distance* after the *AOE*, z_{Rf}, we obtain:

$$z_{Rf} = \frac{z_{Ri} f^2}{f^2 + z_i^2 - 2 z_i f + z_{Ri}^2} \tag{4.9}$$

where z_{Ri} and z_i are respectively the *Rayleigh distance* of the initial beam and the distance between the *AOE* and the initial waist, defined as the origin of the position on the propagation direction.
Fig.(4.14) shows a comparison between the theory and the experimental data, including a linear fit to the latter.

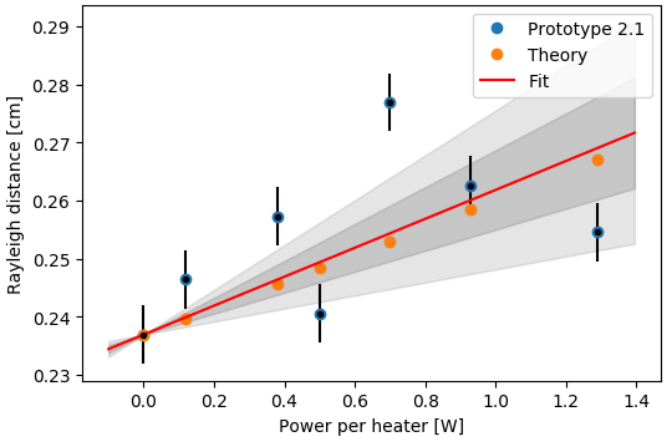

Figure 4.14: Linear fit between experimental data and the theoretical prediction assuming 100% efficiency. We impose to the fit line to pass through the first data point, because it represents the beam with the *AOE* switched off, i.e. our reference value. The two areas coloured with two different shades of gray represent the 1 and 2 sigma confidence intervals. Value above the 100% efficiency theoretical line are obviously non-physical.

Our data seem to be in agreement with 100% efficiency, corresponding to a slope of $0.025 \pm 0.006 cm/W$. However, we can set some lower limits to this value using the uncertainty on the fitting parameters. Considering the best-fit slope minus its error we obtain a percentage of $> 80\%$ at 1 sigma and $> 50\%$ at 2 sigma.
We can compare our values of efficiency with the one obtained with *Prototype 1*.
As mentioned in Sec.(2.1.2), Eq.(1.13) describes the relation between the effective power on the lens and the focal length obtained, independently from the beam used for the experiment. Fig.(2.3) shows the theoretical focal length for 100% efficiency compared to the data of *Prototype 1*. From that image we estimate the efficiency of the old prototype

to be 14%.
In order to compare directly our experimental data to the previous prototype (so using single experimental points instead of the 1 and 2 sigma credible interval of the fit), we need to translate them from values of the *Rayleigh distance* in values for the focal length, which is independent from the beam used, and so comparable with the data from *Prototype 1* and the theory.
Indeed, it is possible to find the focal length of the *AOE* from the *Rayleigh distance* inverting Eq.(4.9):

$$f = \frac{z_i z_{Rf} \pm \sqrt{(z_{Rf} z_{Ri})(z_i^2 + z_{Ri}^2 - z_{Rf} z_{Ri})}}{z_{Rf} - z_{Ri}} \tag{4.10}$$

where we take the solution with the $-$, because when we give it the theoretical values of the *Rayleigh distances* shown in Fig.(4.14) (so with 100% efficiency) we want to obtain the same values found with Eq.(1.13). Trying to compute the $+$ results in values $-1m < f < 0m$ for the focal.
We find the following focal lengths from our experimental data:

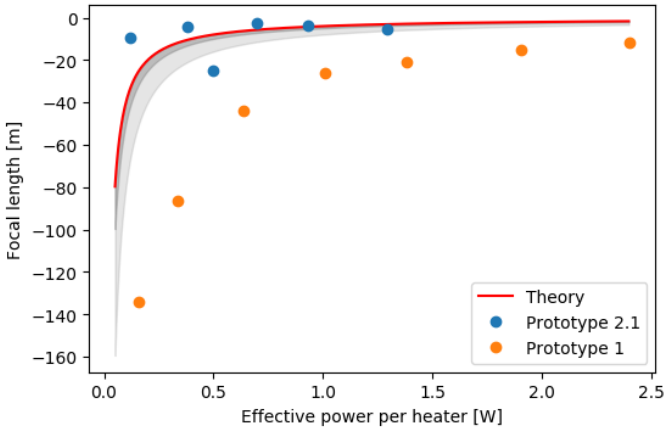

Figure 4.15: Comparison between the theoretical formula for the focal length versus the effective power, *Prototype 2.1* (blue points) and *Prototype 1* (orange points). For clarity we show also the 1 and 2 sigma confidence intervals of our data, plotted as different shades of gray. (*Prototype 1* data taken from: *M. A. Arain, W. Z. Korth, L. F. Williams, R. M. Martin, G. Mueller, D. B. Tanner, D. H. Reitze, "Adaptive control of modal properties of optical beams using photothermal effects", Optics Express, (2010)*)

As expected they are noisy, but again they seem to follow the prediction of the theory with 100% of power absorbed by the lens, so they appear far more efficient than the data from *Prototype 1*.
Since they are this noisy, we can consider the 1 and 2 sigma confidence intervals as representatives of our data, plotted as different shades of gray in Fig.(4.15).

As clearly visible in Fig.(4.15), even the worse estimation at 2 sigma of our *AOE* represents a clear improvement with respect to the previous device.
In terms of increment of thermal efficiency I with respect to *Prototype 1*, defined as:

$$I = \frac{P_{eff}^{(2.1)}}{P_{eff}^{(1)}} \tag{4.11}$$

($P_{eff}^{(i)}$ is the effective power transmitted to the optic and i indicates the number of the prototype) we obtain an increment of $I = 7.15$, considering the fitted value, and $I > 5.71$ (1σ) and $I > 3.57$ (2σ), considering the lower limits discussed above.

Chapter 5

Conclusions

The mode matching problem plays a main role in all the experiments involving optics or optical cavities, since the optical losses emerging from it can compromise their performances. In particular in ground-based interferometers for *GW*, a well matched cavity allows to implement techniques, such as the vacuum squeezing, able to increase their sensitivity. To do so, low-noise actuators are needed and the thermal ones rise as a solution thanks to their efficiency and reliability.
For this reason, *AOE* have been studied, designed and tested at *UF* since 2010, obtaining excellent results with *Prototype 1.* However, it had an excessively low thermal efficiency, which limited its possibility. In order to solve this issue, we worked on a new project to make it more efficient, while maintaining a good robustness and simplicity of assembly.
Our measurement, even if preliminary, shows an increment of the thermal efficiency of a factor from 3.57 to 7.15, and, above all, an efficiency already near to 100%.

5.1 Structural and Mechanical Aspects

The assembly process of the new *AOE* represents surely a success thanks to its simplicity and robustness. In fact, the new geometry of the holders and their positioning with respect to the heaters allow to precisely control the separation distance between the electrical wires contacting two adjacent contact pads of different heaters, making very easy to achieve a good contact simultaneously on all the contact pads.
The heaters design and realization can also be considered a success, since our pattern allows to achieve a thickness of $1\mu m$ while maintaining an effective resistance of $\approx 20/24\Omega$.

Moreover, the properties of the gold-filled wires are excellent for this application: not only they assure the strength necessary to clamp the wires on the holders, but also they keep the ability to deform following the shape of the lens thanks to their superficial malleability. Probably using pure gold wires would have improved further the contact with the heaters, but the gold-filled have a mechanical advantage on their side, and the two aspect should be weighted one against the other.

In addition, the redesigned holders have improved the usability of the whole support structure of the *AOE*, which turned out to be a simple, but efficient way to regulate the position the the holders.

Even if we used *PEEK* to test the functionalities of our project, our design was kept suitable for a future version made of Macor, which will make the device full-fledge *LIGO*-approved.

5.2 Thermal Efficiency and Uniformity

We demonstrated an increase in thermal efficiency, defined as the ration between the heating power deliver to the lens and the total electrical power provided to the device, of a factor $I = 7.15$, considering the fitted value of efficiency, or $I > 5.71$ at 1σ or $I > 3.57$ at 2σ with respect to *Prototype 1*. This was possible thanks to the direct deposition of the heaters on the lens and to the smart design of the holders, which limit the heat loss by conduction through the structure.
This is another success of this device, since it is expected to require about a fifth of the power compared to *Prototype 1* to create the same $-10m$ lens.

It must be noted that we are not able to verify that the pattern adopted for the heater does indeed result in a heat distribution integrated along the optical axis that is really circularly symmetric. However the improvement in efficiency we obtained is largely independent of the heater pattern, which can be optimized via better modelling (for example using finite element analysis) paired with beam quality measurement.

5.3 Future Works

The *AOE* built, tested and analysed through this thesis represents a substantial step forward in obtaining an efficient device usable in *LIGO* and similar experiments. However, it also needs some further testing to verify and confirm the various aspects underlined in the previous paragraphs. Adding some upgrades, it can be improved even more, becoming more efficient and versatile.
First of all, the device needs to be tested with a bigger beam on the *AOE* in order to obtain less noisy and more reliable data than the ones shown during this thesis. Furthermore, beam quality can be analysed using a scanning cavity or a wavefront sensor [4]. This would also allow to investigate the symmetry of the thermal gradient, which also needs to be better characterised modelling more accurately the pattern of the heaters (if necessary they can also be optimized in order to obtain a better circular symmetry).
Moreover, the ability of the device to compensate some astigmatic defect of the optical elements of the experiment or to correct very precisely the alignment of a beam have to be tested [6]; they represent an interesting and useful possibility of this design.

In addition, the thermal response versus time needs to be evaluated in order to determine the bandwidth of the device; then it can be tested in a feedback loop system able to follow time-dependent deformations of a cavity.
Secondly, there are some mechanical improvements, which can be done on the *AOE*. For example, since the design was maintained suitable for Macor, the first step would be building another version with this material. This would make the device really *LIGO*-compatible and eliminate the temperature limit imposed by *PEEK* (even though other consideration would prevent to push the device to working temperature as high as the $1000°C$ possible with Macor)
Then it must be investigated if pure gold wires, or even better gold-filled wires with a thicker gold layer, if available, can improve further the value and repeatability of the contact resistance between them and the contact pads.

In this thesis we have seen how thermal lensing can be exploited as an important tool to help successfully implement other technologies which can increase the already incredible sensitivity of laser interferometers for the detection of gravitational waves. In particular, it can allow to use efficiently the squeezed vacuum technique to limit the quantum noise of the existing interferometers. In fact, it allow to limit to negligible values all the optical losses coming from the mismatch of the optical cavities of experiments like LIGO and VIRGO.
Apart from the promising scientific results of this work, which I am proud of, this experience at UF was a priceless opportunity to have a sight of what it means to be part of the research world and to try contributing to some bigger achievement, that will be possibly useful for all the scientific community.

Bibliography

Books

[1] M. P. Hobson, G. P. Efstathious, A. N. Lasenby, *General Relativity: An Introduction for Physicists*, Cambridge University Press, (2006)

[2] S. Wienberg, *Gravitation and Cosmology: Principles and Applications of the General Theory of Relativity*, John Wiley & Sons, (1972)

[3] A. E. Siegman, *Lasers*, University Science Books, Sausalito, California, (1986)

Articles

[4] M. A. Arain, W. Z. Korth, L. F. Williams, R. M. Martin, G. Mueller, D. B. Tanner, D. H. Reitze, *Adaptive control of modal properties of optical beams using photothermal effects*, Optics Express, (2010)

[5] Z. Liu, P. Fulda, M. A. Arain, L. F. Williams, G. Mueller, D. B. Tanner, D. H. Reitze, *Feedback control of optical beam spatial profiles using thermal lensing*, Applied Optics, (2013)

[6] M. A. Arain, V. Quetschke, J. Gleason, L. F. Williams,M. Rakhmanov, J. Lee, R. J. Cruz, G. Mueller, D. B. Tanner, D. H. Reitze, *Adaptive beam shaping by controlled thermal lensing in optical elements*, Applied Optics, (2007)

[7] Alan Weinstein, *Advanced LIGO Optical Configuration and Prototyping Effort*, California Insitute of Technology, Pasadena, CA (2007)

[8] B. P. Abbott, R. Abbott, T. D. Abbott, M.R. Abernathy, ... , C. Zhao, M. Zhou, Z. Zhou, S. E. Zuraw, J. Zweizig, *Observation of Gravitational Waves from a Binary Black Hole Merger*, Physical Review Letters, (2016)

[9] B. P. Abbott, R. Abbott, T. D. Abbott, M.R. Abernathy, ... , C. Zhao, M. Zhou, Z. Zhou, X. J. Zhu, M. E. Zucker, S. E. Zuraw, J. Zweizig, *Exploring the Sensitivity of Next Generation Gravitational Wave Detectors*, LIGO Public Document LIGO-P1600143, (2016)

[10] B. Abbott et al., *GW170817: Observation of Gravitational Waves from a Binary Neutron Star Inspiral* – Physical Review Letters 119 (2017) (DOI: 10.1103/physrevlett.119.161101)

Proposals

[11] https://www.elisascience.org/files/publications/LISA_L3_20170120.pdf

Others

[12] Logbooks made through years and written by multiple authors; they are accessible from *UF* labs

[13] Sheon S. Y. Chua, *Quantum Enhancement of a 4km Laser Interferometer Gravitational-Wave Detector*, PhD Thesis for the degree of Doctorate of Philosophy Physics at the Australian National University, (2013)

[14] T. R. Corbitt, *Quantum Noise and Radiation Pressure Effects in High Power Optical Interferometers*, Submitted to the Department of Physics in partial fulfilment of the requirements for the degree of Doctor of Philosophy in Physics at the Massachusetts Institute of Technology, (2008)

Websites

[15] *LIGO Scientific Collaboration website*, http://www.ligo.org/index.php/

[16] *LIGO Caltech website*, https://www.ligo.caltech.edu/

[17] *UF LIGO Group website*, http://dc.phys.ufl.edu/ligo/#home/main/

[18] *RP Photonics website*, https://www.rp-photonics.com/

[19] *SCHOTT^{TM} website*, http://www.us.schott.com/english/index.html/

This thesis represents the final aim of these years of study in Padova. Surely, it was not easy to arrive here, but, finally, I am standing on the goal line. So, before taking the last step and begin a new journey, I want to thank all people that have shared the way with me.

Firstly, my family: my father Alessandro*, my mother* Rita*, my sister* Alessia *and my brother* Tommaso*, that have always sustained me in all the aspects of my life and have known how to give fundamental pieces of advise at the right moment to lead me on the right path.*

Secondly, my "university friends": Michele*,* Lorenzo*,* Davide*,* Gianmarco*,* Mirko*,* Giorgio *with whom I passed the most beautiful moments in my university life and, as someone said, with whom "I had precious discussions".*

I also want to thank all the other friends, that I will not list out because, lucky me, they are too many.

I want to thank all people that made possible the unique opportunity of working at University of Florida *and all people that has worked with me there, helping me when I needed. In particular,* Prof. J. P. Zendri*,* Prof. D. Tanner*,* Prof. G. Mueller*,* Reid *and* Nicholas*. A special mention goes to* Michele *with whom I shared basically all good and bad things of living abroad. Obviously an honourable mention goes to* Dr. G. Ciani*, that has always been the right person to ask how to solve any kind of problem that arose during the development and writing of this work.*

Last but not least, I want to thank my other half Alessandra*, with whom I passed the most beautiful five years of my life. You have always known how to cheer me up in bad moments and how to make good ones even better.*